# *Scientific Contributions II*

## ▷ Biostructures and Radiation

# Secondary Structure and $Pd^{(II)}$ Coordination in S-Layer Proteins from *Bacillus Sphaericus* Studied by Infrared and X-Ray Absorption Spectroscopy

**K. Fahmy**, M. Merroun[1], K. Pollmann[1], J. Raff[1], **O. Savchuk**, C. Hennig[1], S. Selenska-Pobell[1]

**Published in Biophys. J. 91 (2006) 996-1007 and Biotechnol. Adv. 24 (2006) 58-68**

**Abstract**

The S-layer of *Bacillus sphaericus* strain JG-A12, isolated from a uranium-mining site, exhibits a high metal-binding capacity. This property has allowed the use of this and other S-layers as self-assembling organic templates for the synthesis of nano-sized heavy metal cluster arrays. However, little is known about the molecular basis of the metal protein interactions and their impact on secondary structure. We have studied the secondary structure, protein stability, and $Pd^{(II)}$ coordination in S-layers from the *B. sphaericus* strains JG-A12 and NCTC 9602 to elucidate the molecular basis of the metal nanocluster growth. Fourier transform infrared (FTIR) spectroscopy reveals similar secondary structures, containing $\approx 35\,\%$ $\beta$-sheets and little helical structure. pH-induced IR absorption changes of the side chain carboxylates evidence a remarkably low pK $< 3$ in both strains and a structural stabilisation when $Pd^{(II)}$ is bound. The COO– stretching absorptions reveal a predominant $Pd^{(II)}$-coordination by chelation / bridging by Asp and Glu residues. This agrees with XANES and EXAFS data revealing oxygens as coordinating atoms to $Pd^{(II)}$. The additional participation of nitrogen is assigned to side chains rather than to the peptide backbone. These side chains are thus prime targets for the design of engineered S-layer-based nanoclusters.

**Results and Discussion**

In the present study [1], extended X-ray absorption fine structure (EXAFS), X-ray absorption near edge structure (XANES), and FTIR spectroscopy were used to analyse the general features of the complexation of $Pd^{(II)}$ within the large number of binding sites of the native S-layer proteins of the strains *Bacillus sphaericus* JG-A12 and NCTC 9602. Specifically, the predominant chemical elements involved in the complexation are identified and their location within side chain or backbone groups is addressed. In addition, the secondary structure and pH-dependent structural transitions of these proteins were studied, because the organisms are specifically adapted to a low pH environment. Experiments were designed to investigate the function of carboxylates in metal protein interactions in these S-layers which are rich in Asp and Glu residues found to be specifically involved in metal protein interactions. Additional coordination by nitrogen is likely to also originate in side chain interactions rather than coordination to the peptide backbone.

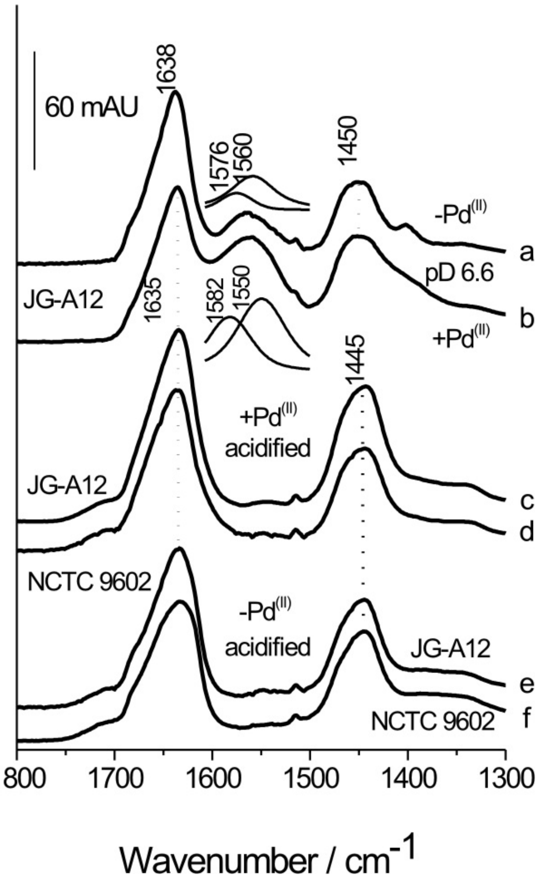


**Fig. 1** *FTIR spectra of S-layers of B. sphaericus strain JG-A12 and NCTC 9602 measured in $D_2O$. a) Spectrum of JG-A12 at pH 7, metal-free. b) Spectrum of JG-A12 at pH 7, $Pd^{(II)}$-bound. Note the broadening of the 1400 $cm^{-1}$ absorption (sym. COO– stretching) and the increase of the $\approx$1560 $cm^{-1}$ absorption (antisym. COO– stretching) as compared to a). The antisymmetric COO- stretching modes where fitted by two components absorbing at 1576 and 1560 $cm^{-1}$ (inset). Besides the strong absorption enhancement, the salient effect of $Pd^{(II)}$ binding is the 10ß,$cm^{-1}$ downshift of the 1560 $cm^{-1}$ absorption, whereas the upshift of the high frequency part is less pronounced. c) Absorption of JG-A12 in the $Pd^{(II)}$-bound state acidified with DCl. d) Absorption of NCTC 9602 in the $Pd^{(II)}$-bound state acidified with DCl. Note the absence of residual absorption in the 1560-1570 $cm^{-1}$ range and the lack of pH sensitivity in the amide II' mode (1450 $cm^{-1}$) in c) and d) as compared to a) and b). e) Absorption of JG-A12 in the metal-free state acidified with DCl. f) Absorption of NCTC 9602 in the metal-free state acidified with DCl. Note the correspondence of the amide II' modes in c) and e) and in d) and f.*

[1] *Institute of Radiochemistry, FZD*

Fig. 1 shows the pH and Pd sensitivity of the antisymmetric carboxylate vibrations around $1560\,cm^{-1}$ in $D_2O$, i.e. free of overlap from amide modes. The absorption intensity increases drastically upon $Pd^{(II)}$ binding and the centre of the antisymmetric stretching frequency shifts from 1567 to $1558\,cm^{-1}$ in the S-layer of *B. sphaericus* JG-A12 (Fig. 2 (a) and (b)), characteristic of carboxylates that chelate a metal ion [2, 3, 4]. Thus, bidentate coordination appears to be the predominant $Pd^{(II)}$ binding mode in the S-layer of strain JG-A12. The lack of a significant shift of the antisymmetric $COO^-$ stretching mode in NCTC 9602 suggests that a bridging coordination is more prevalent in this strain.

Fig. 2 shows the XANES regions of the XAS spectrum obtained with the $Pd^{(II)}$-bound S-layer from strain JG-A12 and for reference compounds containing two oxidation states of palladium: $Pd^{(II)}$ (PdO, $[Pd(NH_3)_4]Cl_2$, $PdCl_2$, $Na_2PdCl_4$) and metallic Pd (0.025 mm thick palladium foil). Comparison of the experimental spectrum to the reference spectra clearly shows that Pd is present as $Pd^{(II)}$ in the Pd-loaded S-layer protein sample because the two absorption maxima (ca. 24360 and ca. 24380 eV) characteristics of metallic Pd (feature marked (a) in Fig. 5) are absent. The fine structure of XANES of the Pd-loaded S-layer resembles that of $[Pd(NH_3)_4]Cl_2$ and PdO, indicating that Pd-O and Pd-N are the predominant bonds that contribute to the metal protein binding. The XANES data indicate that oxygen and nitrogen are the predominant groups that coordinate $Pd^{(II)}$ in the S-layer of JG-A12. Their relative contributions were calculated to correspond to a mixture containing 55 % of Pd-O and 45 % of Pd-N bonding.

In summary, we have shown that carboxylates of Asp and Glu residues exhibit an unusually low pK and are coordination sites for $Pd^{(II)}$ in the two related *B. sphaericus* strains JG-A12 and NCTC 9602 which become structurally stabilised by the heavy metal. Acidic amino acids and probably nitrogen-bearing side chains are thus prime targets for the site-directed modification of S-layer properties such as metal-binding capacity and secondary structure stability which are relevant to metallisation-based biotechnological applications.

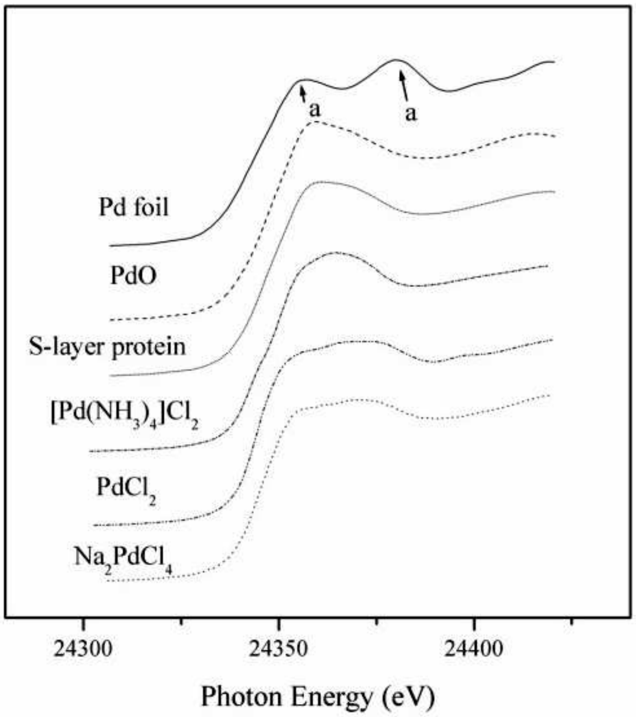


**Fig. 2** *Pd K-edge XANES region of EXAFS spectra of Pd-loaded S-layer protein of B. sphaericus JG-A12 and reference compounds (Pd foil, PdO, $Na_2PdCl_4$, $[Pd(NH_3)_4]Cl_2$, and $PdCl_2$).*


[1] K. Fahmy, M. Merroun, K. Pollmann, J. Raff, O. Savchuk, C. Hennig, S. Selenska-Pobell, Biophys. J. 91 (2006) 996

[2] G.B. Deacon, R.J. Phillips, Coord. Chem. Rev. 33 (1989) 227

[3] M. Nara, M. Tasumi, M. Tanokura, T. Hiraoki, M. Yazawa, A. Tsutsumi, FEBS Lett. 349 (1994) 84

[4] M. Nara, M. Tanokura, T. Yamamoto, M. Tasumi, Biospectroscopy 1 (1995) 47

# Linkage between the Intramembrane H-bond Network around Aspartic Acid 83 and the Cytosolic Environment of Helix 8 in Photoactivated Rhodopsin

N. Lehmann, U. Alexiev[1], **K. Fahmy**

**Accepted for publication in J. Mol. Biol. (2007)**

**Abstract**
Understanding the coupling between conformational changes in the intramembrane domain and at the membrane-exposed surface of the bovine photoreceptor rhodopsin, a prototypical G protein-coupled receptor (GPCR), is crucial for the elucidation of molecular mechanisms in GPCR activation. Here, we have combined FTIR- and fluorescence spectroscopy to address the coupling between conformational changes in the intramembrane region around the retinal and the environment of helix 8, a putative cytosolic surface switch region in class-I GPCRs. Using FTIR / fluorescence cross-correlation we show specifically that surface alterations monitored by emission changes of fluorescein bound to $Cys^{316}$ in helix 8 of rhodopsin are highly correlated with (i) H-bonding to $Asp^{83}$ proximal of the retinal Schiff base but not to $Glu^{122}$ close to the $\beta$-ionone and (ii) with a MII-specific 1643 cm−1 IR absorption change, indicative of a partial loss of secondary structure in helix 8 upon MII formation. These correlations are disrupted by limited C-terminal proteolysis but are maintained upon binding of a transducin $\alpha$-subunit ($G_{t\alpha}$)-derived peptide, which stabilizes the MII state. Our results suggest that additional C-terminal cytosolic loop contacts monitored by an amide II absorption at 1557 $cm^{-1}$ play a functionally crucial role in keeping helix 8 in the position in which its environment is strongly coupled to the retinal-binding site near the Schiff base. In the intramembrane region, this coupling is mediated by the H-bonding network that connects $Asp^{83}$ to the NPxxY(x)F motif preceding helix 8.

**Results and Discussion**
We have investigated the coupling of receptor domains in the hydrophobic core of rhodopsin to surface-exposed regions, particularly to the environment of helix 8 and its C-terminal extension [1]. Changes in the helix 8 environment where specifically monitored by emission from fluorescein linked to $Cys^{316}$ in helix 8. The time evolution of the C=O stretching modes of protonated $Asp^{83}$ and $Glu^{122}$ after MII formation served as sensors of the relaxation of the internal H-bond networks in FTIR difference spectra recorded at defined time intervals after photoactivation. The fluorescence time trace recorded over 15 min was transformed in frequency domain and correlated pairwise with the transform of the absorption changes at each wavenumber using OPUS 2-D-correlation software.

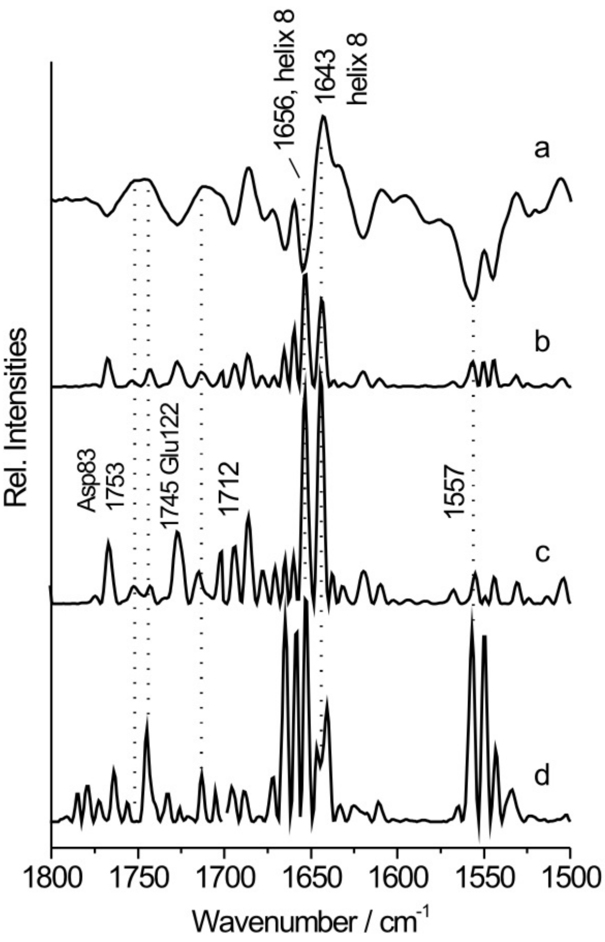


**Fig. 1** *Cross-correlational analysis of IR-absorption changes with fluorescence emission from fluorescein at* $Cys^{316}$. *a) MII difference spectrum of fluoresceine-labeled WMs. b) Squared* $2^{nd}$ *derivative of the spectrum in (a). Data evaluation is based on* $2^{nd}$ *derivatives, which resolve overlapping bands. The* $2^{nd}$ *derivatives were further squared to generate purely positive bands. c) Squared amplitudes of the synchronous correlation of fluorescence changes from the label in helix 8 with the temporal changes in the* $2^{nd}$ *derivative IR spectra measured over 15 min. d) Squared amplitudes of the corresponding asynchronous correlation. The amplitudes, of the absorption changes above 1700* $cm^{-1}$ *have been enlarged by a factor of 10. Spectra are scaled such that* $2 * R^{1/2}$ *equals* $\Delta k$ *in percent of k, with* $\Delta k$ *the rate difference between fluorescence and IR-absorption change, k the average rate of both changes, and R the ratio of a peak in d) versus c). The tentative assignment of helix 8 bands correlated with the fluorescence of the label in helix 8 is indicated.*

[1] *FU Berlin*

Fig. 1 (c) and (d) display the squared synchronous and asynchronous spectrum, respectively, obtained. IR-bands that are strongly correlated with the emission of fluorescein at helix 8 exhibit a small or no amplitude in the asynchronous spectrum, but are present in the synchronous spectrum. Among the amide I modes, this is particularly the case for the MII-characteristic absorption at $1643\,\mathrm{cm}^{-1}$ (Fig. 4 (c) and (d)), which has the lowest ratio R of squared amide I amplitudes in the asynchronous versus the synchronous spectrum. It is thus caused by a secondary-structural change, which evolves in almost perfect concert with alterations in the molecular environment of $\mathrm{Cys}^{316}$. This strong correlation is surpassed only by the absorption of the C=O stretching mode of $\mathrm{Asp}^{83}$ in MII (1750-$1760\,\mathrm{cm}^{-1}$), which is almost completely restricted to the synchronous spectrum. In contrast, the intensity in the absorption range of the C=O stretching mode of $\mathrm{Glu}^{122}$ (1740-$1750\,\mathrm{cm}^{-1}$) exhibits a 20-fold larger $R$ than the $1643\,\mathrm{cm}^{-1}$ band. The temporal difference in the H-bond changes around the two carboxylates shows that they are (i) coupled to disjunct H-bond networks and (ii) they sample unsynchronized conformational relaxations in the respective protein domains. The kinetic distinction between both domains relative to the helix 8 environment suggests the existence of "modular reaction domains" with network-1 (connecting helices 1 ($\mathrm{Asn}^{55}$), 2 ($\mathrm{Asp}^{83}$), and 7 ($\mathrm{Ala}^{299}$, $\mathrm{Asn}^{302}$)) being important for the long-range coupling of the retinal-binding site to a specific G-protein-activating interface. The cross-correlation data fully agree with peptide-derived models that employ partial unwinding of helix 8 during GPCR activation [2, 3], thus giving rise to the fluorescence change of the label and to the $1643\,\mathrm{cm}^{-1}$ absorption increase in MII and the corresponding loss of helical structure of the dark state accounting for part of the negative band at $1656\,\mathrm{cm}^{-1}$.

The different correlations of the H-bonds to $\mathrm{Asp}^{83}$ and $\mathrm{Glu}^{122}$ with the fluorescence from the label in helix 8 is remarkable. We propose that the intramembrane H-bond network connected to $\mathrm{Asp}^{83}$ represents chromophore-protein interactions that are essential predominantly for transmitting intramembrane conformational changes to the cytosolic face via helix 8 movements and that $\mathrm{Glu}^{122}$ senses chromophore-protein interactions that are essential for specific retinal binding. The proposed distinction between mainly activity-promoting ligand protein interactions in the $\mathrm{Asp}^{83}$ / Schiff base environment and mainly specificity-defining interactions around the $\mathrm{Glu}^{122}$ / $\beta$-ionone ring agrees with the almost normal initial rate of MII formation in rhodopsin containing acyclic retinal[45] and is paralleled by the conservation pattern of the two carboxylic acids. $\mathrm{Asp}^{83}$ is strictly conserved throughout the rhodopsin-like class of GPCRs carrying the $\mathrm{NPxxY(x)_{5,6}F}$ motif, whereas homologues of $\mathrm{Glu}^{122}$ are restricted to opsins. Thus, the linkage of the helix 8 environment to the H-bond network that contains $\mathrm{Asp}^{83}$ may represent a conserved functional connectivity from the ligand-binding site to the Gt-interacting domain in class I GPCRs.

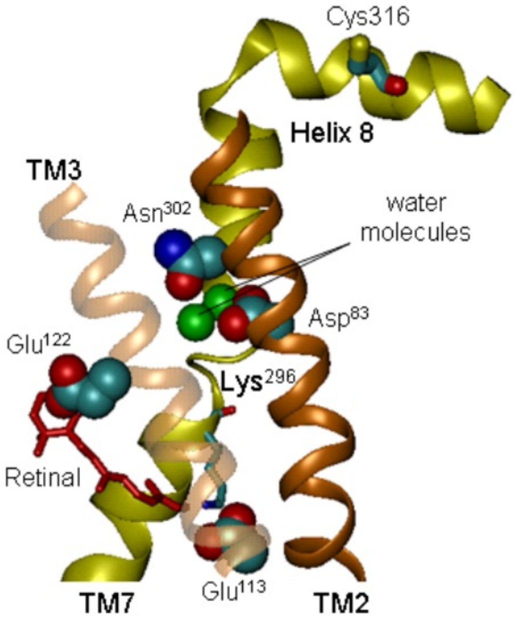


**Fig. 2** *Rhodopsin structure showing the different intramembraneous regions sampled by the internal carboxylic acids $Asp^{83}$ and $Glu^{122}$. The cross-correlation data indicate that the water molecules connecting $Asp^{83}$ with $Asn^{302}$ provide the critical H-bonds that couple the helix 8 environment through the $NPxxY(x)_{5,6}F$ motif to $Asp^{83}$ in H-bond network-1, rather than to the H-bond network-2 around $Glu^{122}$ in the vicinity of the $\beta$-ionone ring. TM designates the intramembraneous helices.*

[1] N. Lehmann, U. Alexiev, K. Fahmy, J. Mol. Biol. 2006 Dec 15; [Epub ahead of print]

[2] S. Mukhopadhyay, S.M. Cowsik, A.M. Lynn, W.J. Welsh, A.C. Howlett, Biochemistry 38 (1999) 3447

[3] S. Mukhopadhyay, H.H. McIntosh, D.B. Houston, A.C. Howlett, Mol. Pharmacol. 57 (2000) 162

# Physical Properties of the Transmembrane Segment 3 of Rhodopsin

S. Madathil, G. Furlinski, K. Fahmy

**Published in Biopolymers 82 (2006) 329-333**

**Abstract**
Activation of G protein-coupled receptors (GPCRs) originates in ligand-induced protein conformational changes that are transmitted to the cytosolic receptor surface. In the photoreceptor rhodopsin, and possibly other rhodopsin-like GPCRs, protonation of a carboxylic acid in the conserved E(D)RY motif at the cytosolic end of transmembrane helix 3 (TM3) is coupled to receptor activation [1]. Here, we have investigated the structure of synthetic peptides derived from rhodopsin TM3. Polarized FTIR-spectroscopy reveals a helical structure of a 31-mer TM3 peptide reconstituted into PC vesicles and helical structure is also observed for the TM3 peptide in detergent micelles and depends on pH especially in the C-terminal sequence. In addition, the fluorescence emission of the single tyrosine of the D(E)RY motif in the TM3 peptide exhibits a pronounced pH sensitivity that is abolished when Glu is replaced by Gln demonstrating that protonation of the conserved Glu side chain affects the structure in the environment of the D(E)RY motif of TM3. The pH-regulation of the C-terminal TM3 structure may be an intrinsic feature of the E(D)RY motif in other class I receptors allowing the coupling of protonation and conformation of membrane-exposed residues in full length GPCRs.

**Results and Discussion**
In this study [2] the synthetic peptide TM3 (108-138), derived from helix 3 of rhodopsin was reconstituted in to large unilamellar PC vesicles and detergent micelles in which they exhibit typical alpha helical structure. The IR data gathered from the pH change of the TM3 peptide reveals that the amide 1 bond is found at $1655\,\mathrm{cm}^{-1}$ with a slight shoulder at $1624\,\mathrm{cm}^{-1}$ which is more pronounced at pH 8.8 than at pH 2. Acidic pH favors the helical content and the IR data imply the solvent accessibility of Glu$^{134}$, the only titratable group in the accessed range. The pH induced structural transition was further addressed by the fluorescence of Tyr$^{136}$ in detergent solubilised TM3. The pH dependent spectral changes of Tyr$^{136}$ were recorded and a pKa of  6 of the acid-induced decrease of tyrosine emission is found, whereas emission increases again below pH 4. The pH dependence is almost completely abolished when Glu$^{134}$ is replaced by Gln. In combination with FTIR data, the results show that the conserved carboxylate is solvent-accessible in micelles and confers pH sensitivity to the TM3 peptide secondary structure specifically in the environment of the D(E)RY motif. In conclusion we have proved here that TM3 sequence forms an $\alpha$-helix in the absence of helix packing interactions and the measured tilt of the helical axis argues that the C- and the N- termini localize at the lipid bilayer. The demonstrated protonation of Glu$^{134}$ thus occurs at the hydrophobic / hydrophilic phase boundary in lipids or detergent micelles and in the latter the protonation state of Glu$^{134}$ affects the neighboring tyrosine and stabilizes the helical TM3 structure. We hypothesize that the conserved hydrophobicity profile around the D(E)RY motif renders the carboxylate to be a critical side chain for the pH- dependent positioning of TM3 by generating a more contigious hydrophobic region at the TM3 C-terminus in the protonated site.

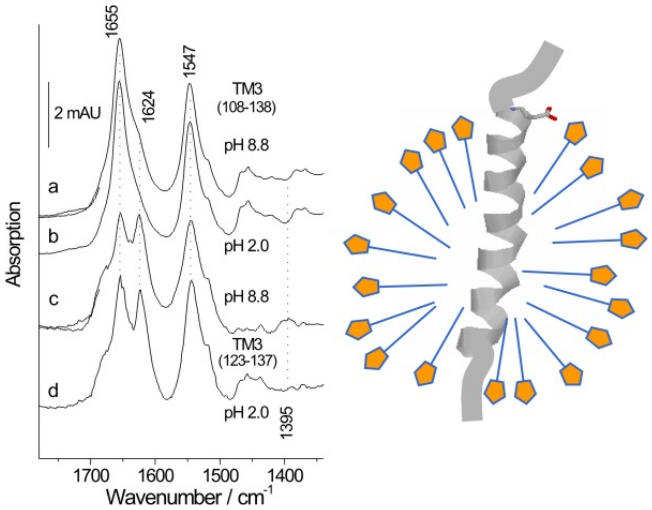


**Fig. 1** *ATR-FTIR-spectra of detergent- solubilised TM3 peptides. TM3 of rhodopsin (108-138) in 5% dodecylmaltoside at pH 8.8 (a) and pH 2 (b). Absorption of a TM3 fragment (123-137) at pH 8.8 (c) and at pH 2 (d). The sketch to the right shows the proposed peptide structure in the micelle with the titratable carboxylate which induces local helicity upon protonation.*

[1] K. Fahmy, T.P. Sakmar, F. Siebert, Biochemistry 39 (2000) 10607-10612.
[2] S. Madathil, G. Furlinski, K. Fahmy, Biopolymers. 82 (4) (2006 ) 329-333

## Structure-Function Relationship of Actin-Flavonoid Interactions

**S. Madathil, K. Fahmy**, M. Böhl[1], F. Pfennig[1], H.O. Gutzeit[1], S. Tietze[2], A. Sokoll[2], J. Apostolakis[3]

**Submitted to Biophys. J.**

**Abstract**
Flavonoids are secondary plant metabolites that have been widely studied because of their potential health benefits and their ubiquitous appearance in the human diet [1]. Based on the identification of actin as a target protein [2] for the flavonol quercetin, the biochemical parameters of this interaction were studied using fluorescence and infrared spectroscopy and the binding parameters of related flavonoids were compared. Furthermore, the potential biological relevance of the flavonoid/actin interaction in the cytoplasm and the nucleus was addressed using an actin polymerisation and a transcription assay, respectively. While flavonols inhibit actin functions, the structurally related epigallocatechin tends to promote actin activity in the two test systems. Infrared spectroscopy evidence suggests that flavonoid-specific conformational changes of actin mediate the different effects on its activity. Docking studies provide models of flavonoid binding and biological activity for the different known binding sites in actin.

**Results and Discussion**
In this study, the intrinsic quenching of tryptophan fluorescence of actin when treated with a set of flavonoids was used as a marker of actin-flavonoid complex formation. The data suggest that the actin forms stable complexes with flavonoids and the flavonoids from different subgroups show similar quenching efficiencies and exhibit $K_d$ values that differ only by 10-30 % within and between subclasses depending on the specific hydroxyl group substitution pattern. A pyrenyl-actin-based fluorescence assay has been developed to study the influence of flavonoids on actin polymerisation. The magnitude of the effect of flavonoids on polymerisation and transcription follows the same order. The impact of two flavonols, quercetin and epigallocatechin exhibiting opposite effects in the actin polymerisation assays, on the conformational equilibrium and structural stability of actin under most native-like conditions was assessed by FTIR spectroscopy. The data show that both flavonols bind to actin in the ATP- and $Ca^{2+}$b-bound state and induce distinct and flavonol-specific structural changes. A detailed docking analysis using four different structures of actin [3] pointed out tetramethylrhodamine as a realistic candidate for flavonol binding in actin. Based on our results we show that structurally related flavonoids bind to actin and affect its biological function in a dose and structure dependent manner.

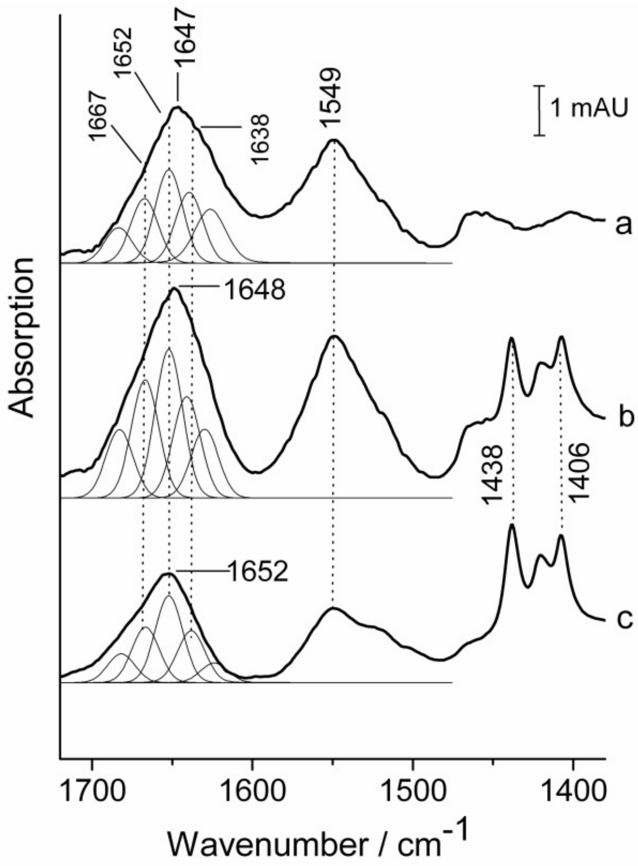


**Fig. 1** *ATR-FTIR spectra in the amide I and II spectral range of free and flavanol-bound actin. (a) Actin in the absence of flavanols (b) Actin in the presence of 50 µM epigallocatechin. (c) Actin in the presence of 50 µM quercetin. The amide I contour was fitted by gaussian / lorentzian bands.*

[1] E. Middleton, C. Kandaswami, T.C. Theoharides, Pharmacol. Rev. 52 (2000) 673-751.
[2] M. Böhl, C. Czupalla, S.V. Tokalov, B. Hoflack, H.O. Gutzeit, Anal. Biochem. 346 (2005) 295-299
[3] D.S. Kudryashow, M.R. Sawaya, T.O. Yeates et al., PNAS 102 (2005) 13105-13110.

[1] *TU Dresden*
[2] *Ruhr Univ. Bochum*
[3] *Ludwig-Maximilians Univ. München*

# Structural Properties of the Kinesin "Coiled-Coil Break 1" Region

**S. Madathil, K. Fahmy**, A.H. Crevenna[1], D.N. Cohen[1], J. Howard[1]

**Submitted to Biophys. J.**


### Abstract

Kinesin-1 transports cargo along microtubules. In vivo, several kinesins move a single organelle and it is important that they operate in a coordinated fashion so that they do not interfere with each other. Coordination is thought to be facilitated by flexible domains. The tail of kinesin-1 is predicted to be a coiled-coil with two main interruptions, the swivel (380-442aa) and the hinge (560-624aa). In a gliding assay, [1] deletion of the swivel impaired motor cooperation at large kinesin densities. The torsion elasticity constant ($k$) was measured by analyzing the rotational random motion of microtubules tethered to a glass surface by single kinesin molecules. Removal of the swivel has no effect on the stiffness of the motor ($k = 7 \pm 1\, k_b T/rad$) nor has the removal of the hinge and subsequent tail domains ($k = 8 \pm 1\, k_b T/rad$) when compared to the full length ($9 \pm 3\, k_b T/rad$). The structure and thermal stability of the swivel region was studied by CD, FTIR, and fluorescence spectroscopy of model peptides. The data indicate the existence of secondary structure within the ≈50 central residues in the Swivel flanked by random stretches. Dimer formation between these more stable helical domains of the Swivel in the two kinesin heavy chains may account for the unexpected large torsional rigidity of the Swivel observed here at the single molecule level. We propose that the localized helical propensity in the swivel provides a mechanism for a reversible structural transition that generates the required flexibility at high motor densities by strain-dependent helix unwinding.


### Results and Discussion

The functional studies carried out in this project convincingly show that the Coiled-Coil Break-1 behaves differently from what is expected for a disordered structure: (1) its torsion elasticity is higher than predicted by the WLC model, (2) its deletion doesn't cause an increase of stiffness. These results suggest that a certain degree of secondary and / or tertiary structure may be present in this region which was experimentally demonstrated by the structural studies on the five 30 aa long overlapping pieces of synthetic model peptides derived from this region. CD spectroscopy at 20$^o$C revealed that the peptides 3 and 4 (corresponding to the central part of Coiled-Coil Break-1) show characteristic $\alpha$-helical far UV-CD spectra and display the greatest molar ellipticity corresponding to around 70% total helical content. Peptide 1 and 5 have a low percentage of helicity and peptide 2 is the most unstructured one, supporting previous findings. The FTIR data of the most helical peptides 3 and 4 suggest that these helices form coiled-coils [2]. The energetics of the structural transitions of the model peptides, addressed by fluorescence-based thermal unfolding experiments, is in full agreement with the presence of defined secondary structure demonstrated by CD and FTIR spectroscopy. Based on the ensemble of our functional and structural studies we suggest that only at high motor densities the strain exerted on the swivel induces the transition of the structured regions from helical to disordered stretches, thereby providing the required flexibility in a function-dependent manner.

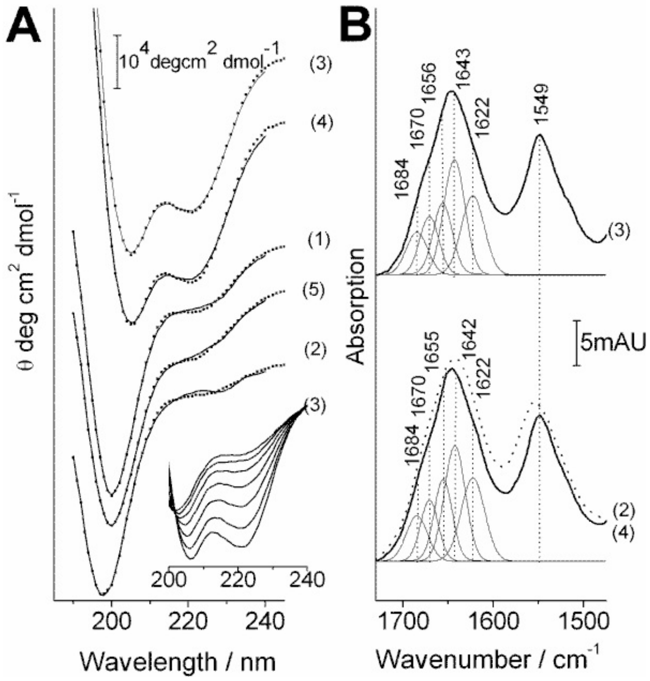


**Fig. 1** *(A) CD spectra of the 5 model peptides at 20$^o$C and the inset shows the CD spectra of peptide 3 from 2-60$^o$C. (B) FTIR spectra of peptide 3 and 4 which form coiled coils and of peptide 2 which is unstructured.*


[1] J. Howard, A.J. Hudspeth, R.D. Vale, Nature. 342 (1989) 154-158

[2] S. Krimm, J. Bandekar. Adv. Prot. Chem. 38 (1986) 181-236


[1] *MPI-CBG Dresden*

# Dynamics of FEL-Light-Induced Changes in Thin DNA Films Observed by Brewster Angle Microscopy

M. Sczepan, G. Furlinski, D. Wohlfarth, W. Seidel, K. Fahmy

**Abstract**

The function of biopolymers is determined by their structural dynamics. Investigation of the structural dynamics is thus important for understanding the processes and superstructures involved in the function of biomolecules. A large number of superstructures is particularly important for DNA function. Our experiments aim at the induction and kinetic analysis of the IR-induced transitions between such states.

In order to observe changes induced in thin DNA films by FEL irradiation, Brewster angle microscopy, which is a proven technique for the evaluation of thin organic films [1] has been employed. If a sample is observed under Brewster angle conditions, small changes in the refractive index of the surface can be detected and thus thin layers on the surface of a substrate or liquid can be made visible. Small changes in the refractive index and thickness of a thin film as a result of structural transitions will induce changes in the reflectivity of the film.

### Results and Discussion

Experiments have been performed using thin layers of DNA (pUC21 plasmid DNA, PlasmidFactory) on ZnSe and $CaF_2$ substrates. The thickness of the layers has been estimated to be 50-800 nm by interference fringe counting in combination with absorbance measurements. These samples were irradiated with FEL light at different wavelengths. Fast changes of reflectivity - following the temporal structure of the FEL light intensity which are followed by slow relaxation processes ($\approx$ 30 ms) were observed (see Fig. 1). Experiments to determine the influence of the micropulse energy (20-100 nJ), film thickness, macro bunch length (200-1200 $\mu$s) and humidity have been performed and revealed a strong influence of these parameters on amplitudes and time constants of the reflectivity variations.

Analysis of the data for films of different thicknesses - especially for films with thicknesses between 50 nm and 150 nm - reveal that changes in the reflectivity on the longer time scale are the result of a decrease in the refractive index of the sample while the fast ($< 30\,\mu$s) changes can be attributed to variations (increase followed by decrease) of film thickness due to heating. A model for the heat transport in the sample has been established, allowing the estimation of the temperature reached in the sample as a function of film thickness and pump power. Estimated temperature jumps were found to be in the 50-500 K range with the equilibrium temperature established within less than 50 $\mu$s. For high film thicknesses and pump intensities resulting in high film temperatures, a more complex behaviour of the reflectivity was observed. In this case, thickness changes - probably as a result of variations in sample hydration - seem to contribute to the slow changes in reflectivity. The changes in the refractive index of the sample can be the result of structural changes (base pair stacking, strand opening [2]) as well as of variations in the hydration state of the DNA [3]. In summary, we have shown that FEL-pulses can induce rapid DNA melting, allowing to observe base pair separation and annealing with a time resulution not accessible by conventional experiments on DNA-structural transitions.

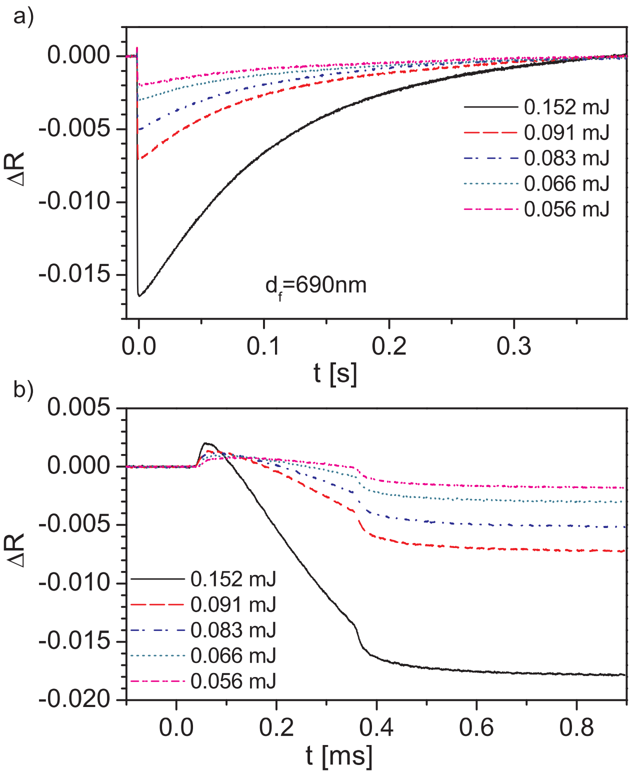


**Fig. 1:** *Change of reflectivity of a DNA film (thickness 690 nm) during and past FEL irradiation in long (a) and short (b) time scale as a function of light intensity/macro bunch energy.*

[1] S. Hénon, J. Meunier, Rev. Sci. Instr. 62 (1991) 936

[2] S. Elhadj, G. Singh, R. Saraf, Langmuir 20 (2004) 5539

[3] S. Weidlich, S.M. Lindsay, A. Rupprecht, Biopolymers 26 (1987) 439

# Identification of Actinide Molecule Complexes by Vibrational Photothermal Beam Deflection Spectroscopy

H. Foerstendorf[1], K. Heim[1], **W. Seidel**, G. Bernhard[1]

**Accepted for publication in J. Nucl. Mat. (2007)**

**Abstract** Photothermal Beam Deflection (PTBD) spectroscopy in the infrared region combines the low detection limits, the surface selectivity of photothermal methods [1, 2] and vibrational spectroscopic information of the sample under investigation [3]. We present first results of model samples containing actinide molecule complexes obtained by PTBD using an FEL as a coherent pump source. The spectra are compared with those obtained by Fourier-transform infrared (FT-IR) spectroscopy.

The setup of the PTBD-FEL experiment is described elsewhere [4]. All samples were prepared as KBr pellets as typically used for FT-IR spectroscopy. PTBD absorption spectra and FT-IR transmission spectra represent the average of 128 scans for each data point and spectrum, respectively. Spectral resolution was 2 - 3 $cm^{-1}$ for PTBD (depending on wavelength) and 4 $cm^{-1}$ for FT-IR spectroscopy.

**Results and Discussion** The infrared spectra of a Np(V)nitrate test sample in the spectral region (880 - 680 $cm^{-1}$) where the $\nu_3$ mode of the $NpO_2^+$ cation can be expected are shown in Fig. 1. A comparison of the spectra demonstrates the high accuracy which can be achieved by the PTBD technique in the infrared region. In this spectral range the $\nu_2$ and $\nu_4$ modes of the nitrate group generally show up as well. In fact, the spectra show three partially overlapping bands at 839, 820 and 755 $cm^{-1}$. Today only a tentative assignment of the bands can be given. From Raman spectroscopic investigation [5] we assign the band at 820 $cm^{-1}$ to the $\nu_3$ mode of the $NpO_2^+$ cation. Consequently, the bands at 839 and 755 $cm^{-1}$ have to be assigned to the $\nu_2$ and $\nu_4$ mode of the nitrate group, respectively.

Fig. 2 presents the spectra of the KBr pellets containing the lowest concentrations of $UO_2(NO_3)_2{\cdot}6H_2O$ which provide a clear vibrational $UO_2^{2+}$ band obtained by PTBD and FT-IR spectroscopy. Again the high accuracy of the spectra demonstrates the applicability of the PTBD technique to identify actinide molecule complexes in solid samples. Although it has been shown that photothermal spectroscopy is capable of measuring absorptions below $10^{-6}$ [1] the dynamic reserve of the PTBD technique in our FEL experiment is in the same order of magnitude as for FT-IR spectroscopy since no well-defined absorption bands of the $\nu_3$ uranyl mode were observed at lower concentrations (data not shown). The limitations are obviously set by the KBr matrix which shows a background absorption over the whole spectral range most probably due to residual water and other possible impurities. However, the quantity of the actinide and the dimension of the sample which is necessary for generating a significant deflection signal is considerably reduced in the PTBD experiment due to its geometrical setup. The generation of the thermal wave and of the deflection signal occurs next to the surface of the sample. This potentially provides access to investigations of natural mineral surfaces in future times.

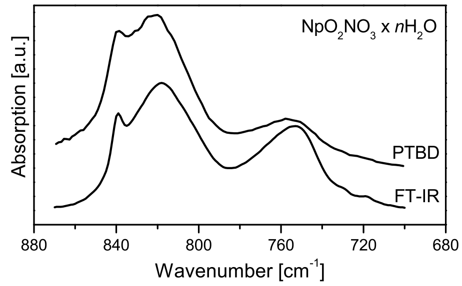


**Fig. 1** *Infrared spectra of the $\nu_3$ mode region of the neptunyl(V) cation measured by PTBD (upper trace) and FT-IR (lower trace).*

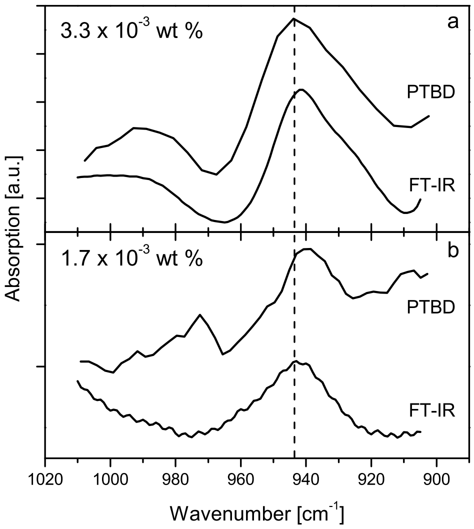


**Fig. 2** *PTBD (upper traces) and FT-IR (lower traces) spectra of the $\nu_3$ mode region of the uranyl(VI) cation at different concentrations of $UO_2(NO_3)_2{\cdot}6H_2O$. (a): 3.3 $\cdot 10^{-3}$ wt % ($\approx$ 150 $\mu$M); (b): 1.7 $\cdot$ $10^{-3}$ wt % ($\approx$ 75 $\mu$M).*

[1] T.D. Harris et al., Appl. Spectrosc. 39 (1985) 28
[2] M. Commandre et al., Appl. Optics 35 (1996) 5021
[3] W. Seidel et al., Eur. Phys. J-Appl. Phys. 25 (2004) 39
[4] H. Foerstendorf et al., J. Nucl. Mat. (2007) in press
[5] A.C. Gregoire-Kappenstein et al., Radiochim. Acta 91 (2003) 665

[1] *Institute of Radiochemistry, FZD*

# Remote Controlled IR-Diagnostic Station for the Rossendorf FELs

**W. Seidel,** R. Jainsch[1], M. Justus, K.-W. Leege[1], D. Proehl[1], H. Weigelt, **D. Wohlfarth**

**Part of Diploma thesis H. Weigelt**

Starting in the summer 2005, FEL beam time has been offered to external users in the frame of the EC funded "Integrating Activity on Synchrotron and Free Electron Laser Science" (FELBE project [1]). It is of great importance for routine user operation at ELBE that, after changing the beam path or after beam interruptions stable operation in all wavelength ranges can be provided within a short time (some minutes). Extensive diagnostics for the optical components of the FEL are very important to achieve fast availability.
We have developed an optical beam diagnostic system (see Fig. 1) to properly characterize and adapt the output of the two FELs (U27 and U100). The present system is compatible with a tuning range from 3 $\mu$m to 150 $\mu$m, and can be extended beyond 150 $\mu$m, if necessary.
The FEL beam from each undulator will be transported separately from the resonator to the diagnostic area through beam pipes using reflective optics. Both lines will be merged on the diagnostic table, which may be purged with dry nitrogen to avoid absorption in air, if necessary. From here both beams follow the same path.
Two flipper mirrors may deflect the beam in a bypass to a plasma switch which reduces the repetition rate from 13 MHz down to 1 kHz (first results see [6]). The switch is based on the principle of photo-induced reflectivity of an optically excited electron-hole plasma [2, 3]. In this way, subsequent FEL micropulses are selected out of the 13 MHz pulse train. An additional focusing mirror ensures the same beam parameters as the direct beam has.
From the main beam, approximately 1-5 percent of the total power is separated by a scraper mirror on a translation stage for wavelength measurement and power monitoring.
The transmitted beam passes an attenuator and can be delivered to 6 optical laboratories. In this attenuator precisely fabricated metal grids diffract a calibrated percentage of power (3, 5, and 3 × 10 dB) out of the beam. The rejected light is absorbed in the walls of the housing. The mode structure and other properties of the transmitted beam including the divergence and the $M^2$ parameters are fully preserved, the polarisation as well [7]. Finally, a non-collinear background-free autocorrelator system is used to determine the length of the ultrashort FEL pulses. We use a CdTe crystal as SHG medium [2, 5] since it is transparent for a wide wavelength range in the infrared.

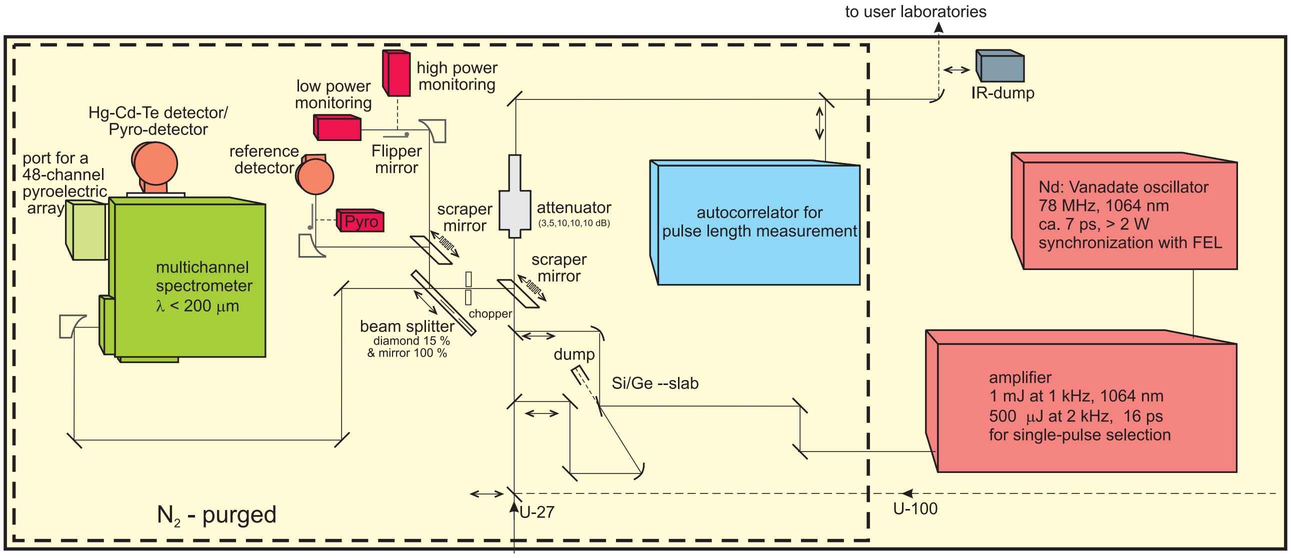


**Fig. 1** *Arrangement of the different optical components and devices on the table.*

[1] *Department of Research Technology, FZD*

The part of the beam deflected by the scraper mirror goes through a synchronized chopper for measurement in CW-mode. Next to this, the outcoupled beam is deflected by a mirror or a diamond beam splitter (350 $\mu$m thick, under 45 degrees, deflection 15 %) at a pneumatic translation stage ( this part of the diagnostic is described in detail in [8]). The beam transmitted through the diamond beam splitter (85 %) is transported to the spectrometer. The spectrum is measured with a Czerny-Turner type spectrometer which contains a turret with three different gratings to cover the whole wavelength range from 3 $\mu$m to about 200 $\mu$m. In the near future the monochromator will be equipped with a 48-channel pyroelectric linear array detector. We use the second side-exit slit equipped with a single Hg-Cd-Te or Ge-Ga detector for measurements with higher sensitivity.

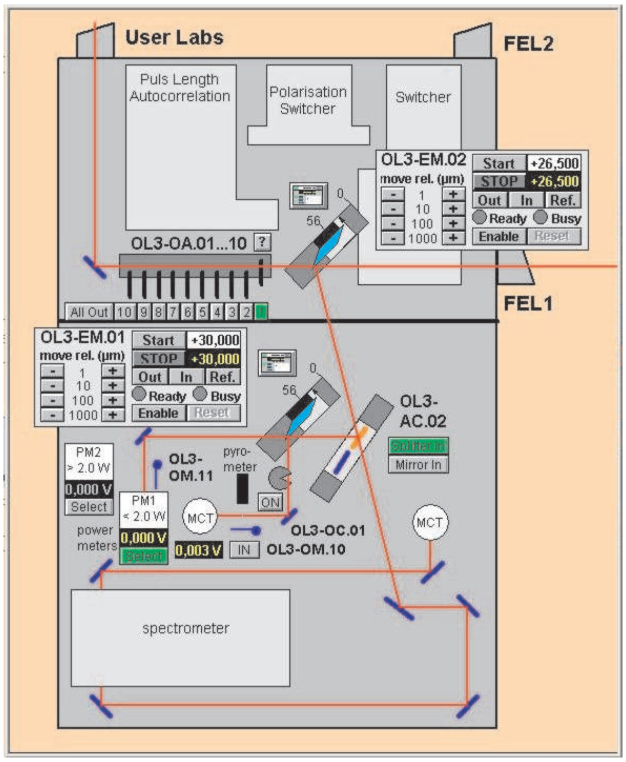


**Fig. 2** *Interface of the remote controlled part of the IR-diagnostic station. One attenuator, two scraper mirrors on stepper controlled stages, one mirror and one beam splitter on a common pneumatic stage, spectrometer and different power meters are indicated. The lines show different paths for the radiation when both scraper mirrors are not entirely within the beam.*

The part reflected from the pneumatic device is distributed with another scraper mirror and two flipper mirrors to different power meters (<2 W and >2 W) and reference detectors (Hg-Cd-Te and pyro-detectors) for monitoring the lasing process (see Fig. 2).
The FEL diagnostic instrumentation has been integrated into the existing Programmable Logic Control (PLC) and Human-Machine-Interface (HMI) environment of ELBE (see Fig. 3). It ensures the access both for operators and users of the FEL. The basic technologies are the WinCC server/client system, the SIMATIK PLC system and distributed I/O by Beckhoff Automation for controlling the pneumatic components (i.e. attenuators), analogue data logging (FEL power, MCT) and other instrumentation. The stepper control drivers for the scraper mirrors are integrated system components, whereby expensive separate controllers could be avoided.

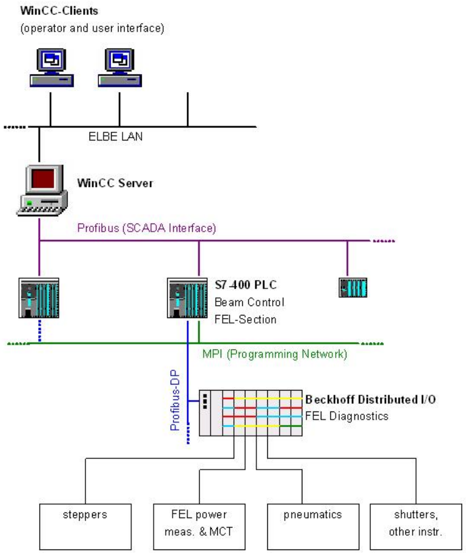


**Fig. 3** *The programmable Logic Control (PLC) and Human-Machine-Interface (HMI) environment of ELBE with the integrated FEL diagnostics instrumentation*


[1] http://www.fzd.de/felbe
[2] J. Xu et al., Opt. Comm. 197 (2001) 379
[3] P. Haar, Ph.D. thesis, Stanford University (1996)
[4] E.H. Haselhoff et al., Nucl. Instr. and Meth. A 358 (1995) ABS28
[5] W. Seidel and D. Stehr, this Report, p. 78
[6] W. Seidel and S. Winnerl, this Report, p. 74
[7] F. Keilmann, SPIE Vol. 666 (1986) 213
[8] H. Weigelt, Diplomarbeit, Hochschule Mittweida, 2006

# Extraction of Single FEL Radiation Pulses Using a Laser-Activated Plasma Switch

**W. Seidel,** S. Winnerl[1]

In order to decrease the average radiation power of the Rossendorf free-electron laser FELBE (FELBE project [1]), as required for certain experiments (high pulse energies but moderate or low average power), the FEL repetition rate can be reduced from 13 MHz to 1 kHz. To this end, plasma switching of FEL radiation pulses was demonstrated for cw operation.
The plasma switch is based on the principle of photo-induced reflectivity by an optically excited electron-hole plasma [2, 3]. Germanium serves as semiconductor material for the switch. The semiconductor was illuminated by a Nd:YAG laser amplifier system (1 kHz, $\lambda = 1064$ nm, $\tau \sim 16$ ps, <1 Watt), generating an electron-hole plasma at the front surface of the semiconductor. The generation of a sufficient plasma density leads to a variation of the optical semiconductor properties for the infrared FEL-radiation (strongly focused and under Brewster's angle of 76°). For realizing the pulse selection the frequencies of both laser sources (FEL and Nd:YAG) were synchronised with RF electronics. For the exact timing of both laser pulses, when they hit the semiconductor, they were detected with a photon-drag detector or a fast pyroelectric detector (FEL) and a photo diode (Nd:YAG) and were adjusted on each other with cables, phase-shifter (trombone) and through moving a precision linear stage. Fig. 1 shows the experimental set-up. A gold mirror served as a reference for determining the reflectivity of the Germanium. The selected FEL pulses were detected by a fast MCT detector with a bandwidth of 20 MHz. Fig. 2 shows the switched pulse in two amplitude scales. The signal from the switch laser (photo diode) is shown in red. From the comparison of the black and blue curves we obtained an amount of dark pulses in the switched beam of about 0.5 % due to the angle of beam spread from the focussing. The time-resolved measurement of the reflectivity yields an exponential decay with a time constant of 590 ps. For the highest value of the Nd:YAG laser amplifier peak fluence of 25 mJ/cm$^2$, a reflectivity of Ge for FEL radiation ($\lambda = 11 \mu m$) of 100 % was achieved (see Fig. 3). We thus succeeded to extract single FEL radiation pulses out of the 13 MHz pulse train, indicating that this plasma switch is most suitable for the Rossendorf FEL. Further examinations will concentrate on achieving similar results for shorter wavelength. To integrate this plasma-switch into the existing diagnostic station we have to build an additional by-pass to the Germanium or Silicon slab which is under Brewster's angle (see [4]). The selected micro pulse will be refocused to the waist parameters outside of the by-pass line and transported to the user stations.

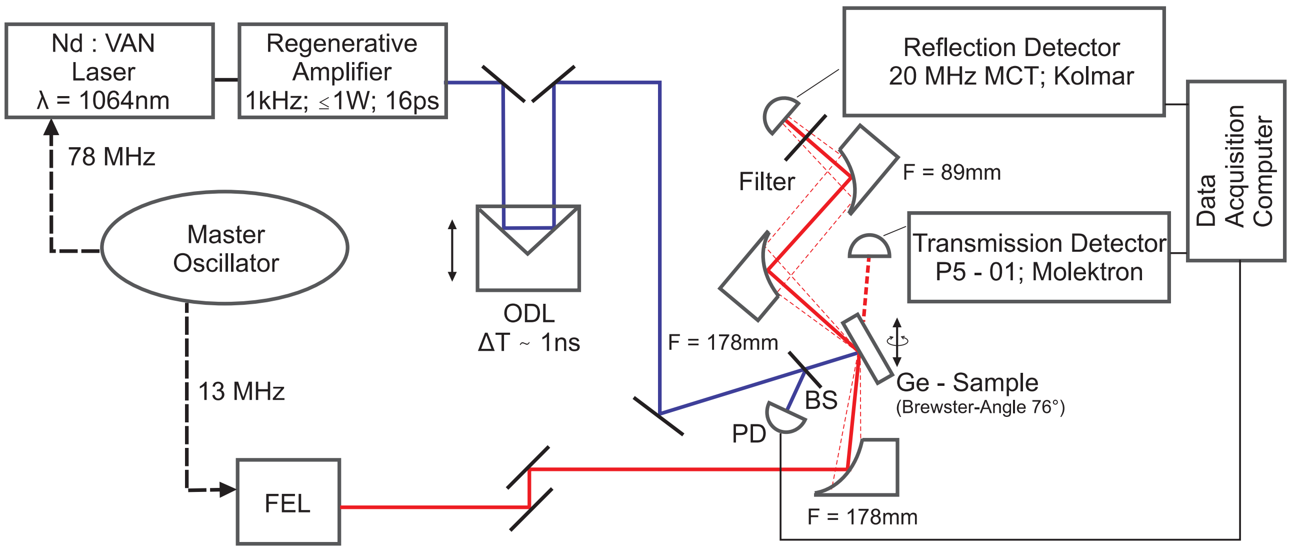


**Fig. 1** *Setup for the plasma switch (for details see above)*

[1] *Inst. of Ion Beam Physics and Materials Research, FZD*

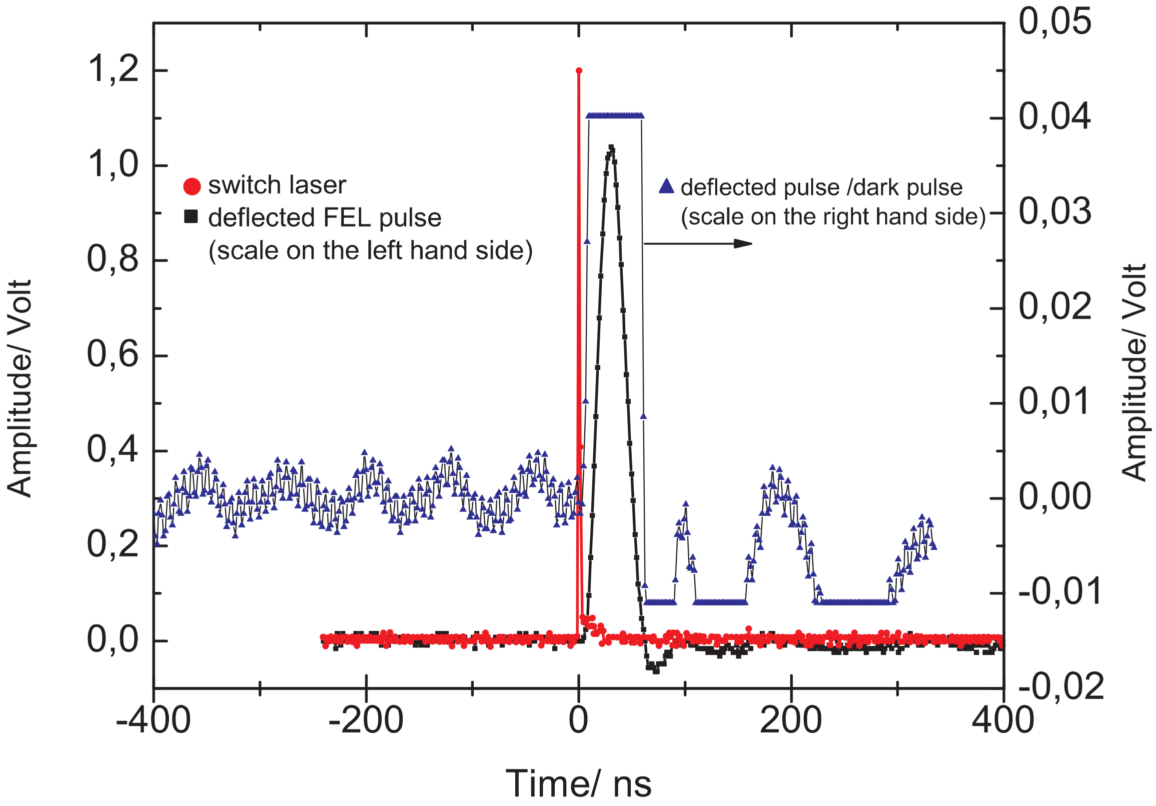


**Fig. 2** *The switched FEL pulse at 11 μm in two different amplitude scales is measured by a fast MCT detector with a bandwidth of 20 MHz. The signal from the switch laser (photo diode) is shown in the curve with circles. From the comparison of the curve with squares and curve with triangles we obtain an amount of dark pulse in the switched beam of about 0.5%.*

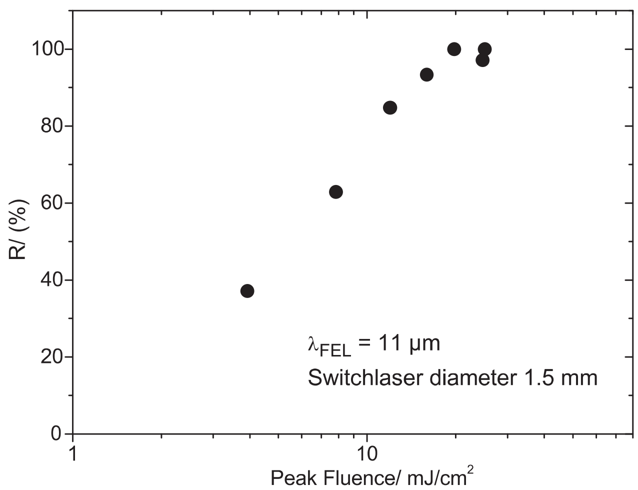


**Fig. 3** *Dependence of reflectivity on the pump-laser peak fluence.*


[1] http://www.fzd.de/elbe
[2] P. Haar, Ph.D. thesis, Stanford University (1996)
[3] E.H. Haselhoff et al., Nucl. Instr. and Meth. A358 (1995) ABS28
[4] W. Seidel et al., this Report, p. 72

# The IR Beam Line from the FELs to the High Magnetic Field Laboratory

**W. Seidel**, A. Winter[1], **R. Wünsch**, S. Zvyagin[2]

An infrared (IR) beam line has been designed which connects the two free-electron lasers (FEL) in the ELBE building [1] with the experimental high magnetic field setup located in the building of the Dresden High Magnetic Field Laboratory (HLD) of the Forschungszentrum Dresden - Rossendorf.

The ELBE FELs produce short, a few picosecond long pulses with a repetition rate of 13 MHz in the medium- and far-infrared region (between 3 and 200 $\mu$m). The repetition rate can be reduced down to 1 kHz. The average radiation power does not exceed a few tens of Watts. The light is linearly polarized. Owing to the large wavelength range we use reflective optics with metal mirrors (gold coated copper or stainless steel). Their reflectivity is larger than 97.5% in the operated wavelength range.

The ELBE-HLD beam line is one of the branches of the general line which delivers the laser light from the IR FELs in the ELBE building to several user laboratories [2]. The beam is guided in pipes which are either evacuated or purged with nitrogen gas. It starts at the outcoupling holes of the resonator mirrors of the U100- and U27-FEL, respectively. The size of the outcoupling holes can be varied. Hole diameters of 2, 4.5 and 7 mm are available for the U100-FEL, while 1.5, 2, 3 and 4 mm holes can be used at the U27-FEL. The beam line has to be adapted to the different outcoupling holes and to the resulting beam divergence which, in addition, depends strongly on the wavelength of the beam. Positions and focal lengths of the used mirrors have been determined to achieve better propagation conditions of the light inside the pipe (including passing through several bottlenecks, e. g. at the window between the preparation room and the magnet lab, waists in the HLD building, etc.). We use the Method of the Equivalent Gaussian Beam [3] to calculate the propagation of radiation along the beam line. Beam radii $w$ are calculated according to the Gaussian beam propagation laws.

First, the beams are transported from the outcoupling holes using separate lines to a diagnostic table in the neighboring room (see Fig. 1). The beam profile has a waist on the diagnostic table. Waist size and position are the same for beams coming from both FELs. The waist position is independent of the wavelength, but the size is proportional to the diameter of the outcoupling hole. The narrow beam size in the vicinity of the waist is used for various beam measurements and modifications. Behind the diagnostic table the beam is distributed between user laboratories using one line. By inserting the plane mirror MH1 into the beam line the beam is becoming bent down to a specific line, guiding the beam via mirrors MH2 - MH4 into a tunnel (27 m long) on the basement level and connecting the ELBE building with the HLD. At the tunnel entrance, the beam is refocused (MH4), becoming a nearly parallel beam. However, diffraction effects increase the IR-beam size much stronger than for visible light. Thus, towards the end of the tunnel the pipe diameter has to be increased to 20 cm. The beam size calculated along the beam line is illustrated in Figs. 2 and 3.

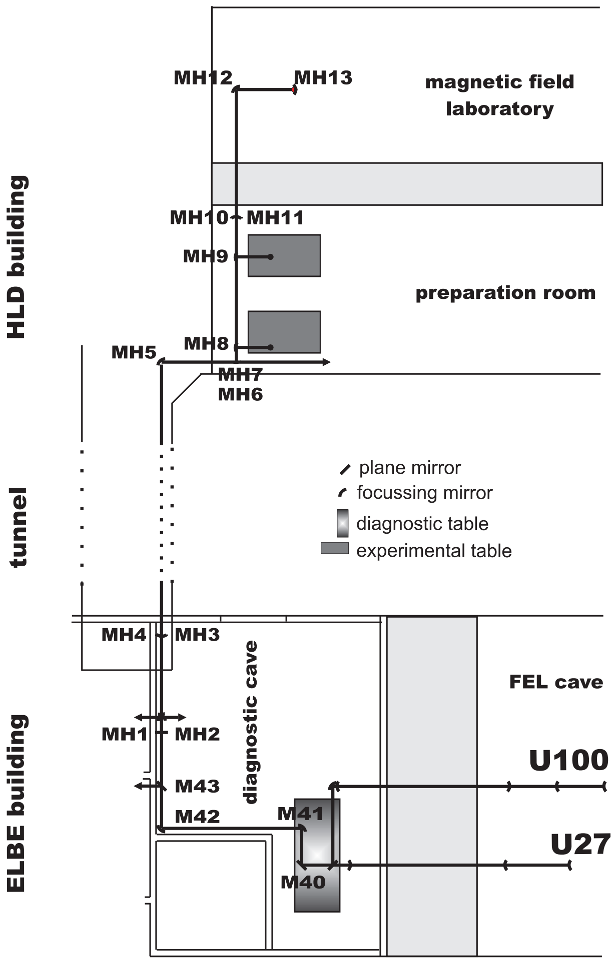


**Fig. 1** *Top view of the beam line from the U100 and U27 FEL in the ELBE building to user stations in the HLD building via diagnostic table and tunnel.*

In the HLD building, the beam has to be deflected within shorter distances. The deflecting mirrors can be used to refocus the beam and to keep the necessary pipe diameter at 10 cm. We assume that a diameter of 3*$w$ is sufficient in this branch of the beam line. Behind the mirror MH5 at the end of the tunnel the beam size decreases clearly. Mirror MH6

[1] *Department of Research Technology, FZD*
[2] *Dresden High Magnetic Field Laboratory (HLD), FZD*

focuses the beam additionally, and deflects it upwards to the experimental preparation room in the ground floor. This mirror can be removed to guide the beam to other laboratories in future. Mirror MH7 brings the beam into horizontal direction 108 cm above floor level. Two removable focusing mirrors (MH8, MH9) allow to deflect the beam to an experimental table, where a beam waist is produced approximately 90 cm behind the mirror. Here, the beam is only a few millimeters wide. The beam going straight on enters the high magnetic field laboratory through a safety window. This window is 46 cm higher than the beam and the beam line is shifted to that level by means of mirrors MH10 and MH11. In the magnet laboratory, a first beam waist is just behind the wall. Here, the beam is between 5 and 15 mm wide ($2^*w$), depending on wavelength and size of the outcoupling hole. The small beam size allows us to insert a diamond window at this place. After the window, the beam is first deflected by the mirror MH12 and then deflected downwards by MH13 and focused onto the entrance of a circular waveguide which finally guides the beam into the cryostat of the high-field magnet. Another diamond window is located 10 cm in front of the entrance into the waveguide at the end of the beam line.

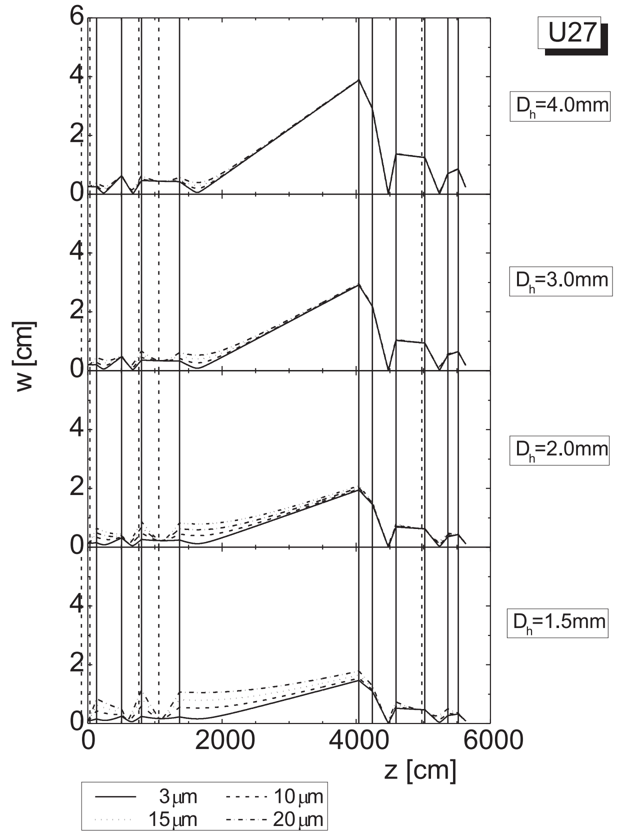


**Fig. 2** *Radius $w$ of the U27 FEL beam calculated from the waist on the diagnostic table to the HLD for different hole sizes $D_\mathrm{h}$ and wavelengths. The vertical solid and broken lines indicate the positions of focusing and plane mirrors, respectively.*

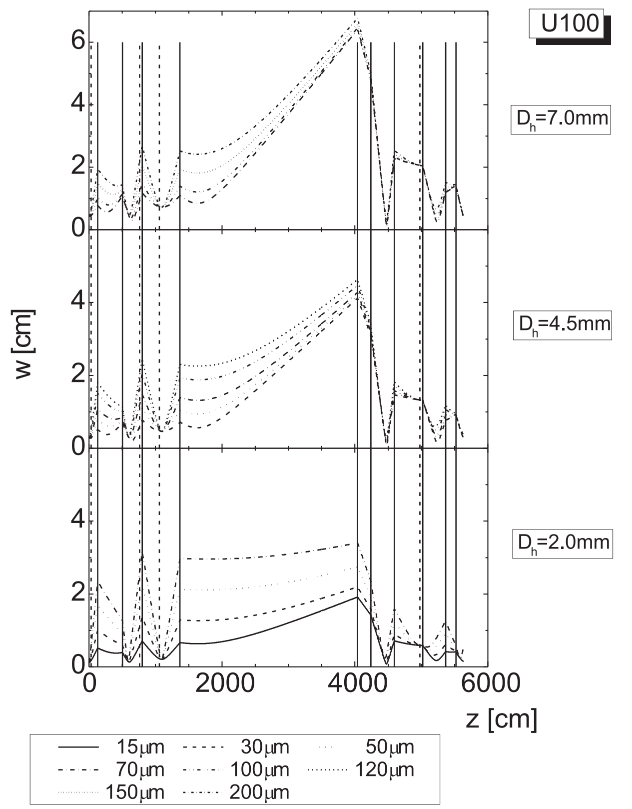


**Fig. 3**. *The same as in Fig. 2 for the beam from the U100 FEL.*

The mirrors are adjusted by means of He-Ne laser beams introduced into the beam line and aligned with the IR-beam. A first alignment beam starts from the FEL resonator. It is used in the laboratories of the ELBE building. Towards the end of the tunnel this beam gets rather wide and fades away. That is why we introduce another He-Ne laser beam into the beam line between mirrors MH2 and MH3. This beam is aligned with the first one and can be used for adjusting the mirrors in the HLD. Furthermore, the HLD users may use this beam for setting up high-field experiments.

A broad range of high-field experiments using the FEL facility at the Forschungszentrum Dresden - Rossendorf can be performed. It includes Electron Cyclotron Resonance in metals and semiconductors; Electron Paramagnetic, Antiferromagnetic and Ferromagnetic Resonances in various magnetic dielectrics; investigation of non-linear parametric processes in materials of functional optics and spintronics, pump-probe experiments on quantum wells, high-resolution time-domain spectroscopy of highly-correlated electron systems (including high-$T_c$ materials, heavy-Fermion systems, etc.).

[1] http://www.fzd.de/elbe, 12.01.2007

[2] Th. Dekorsy et al., Proc. Free Electron Laser Conf. 2002, pp. 35,36

[3] H. Kogelnik, Appl. Opt. **4** (1965) 1562-1569

# Spectral Width and Duration of the IR-Pulses from FELBE

**W. Seidel**, D. Stehr[1]

From a user's perspective, the three valuable characteristics of the free electron laser FELBE (among the wavelength range) are its peak power, variable picosecond optical micropulse length, and variable transform limited spectral bandwidth. Precise control of the FEL optical pulse has been essential for many time-resolved measurements performed at FELBE. The optical pulse length can sensitively be tuned by varying the FEL resonator length with respect to the nominal length resulting from the electron bunch repetition rate. At minimum detuning one yields the highest saturated power and the shortest optical pulse length. By detuning the resonator, the spectral width can be decreased simultaneously increasing the pulse length.

To characterize the ultrashort pulses generated by the FEL we built a non-collinear background-free autocorrelator system. We used a CdTe crystal as SHG medium [1], since it is transparent for a wide wavelength range in the infrared. We measured the autocorrelation function at maximum power in the detuning curve at a wavelength of 11.09 $\mu$m (see Fig. 1) generated in the FEL-U27 [2].

We deduced a pulse duration of 0.89 ps (FWHM), assuming a Gaussian temporal pulse shape. The measured FWHM of the spectrum is approx. 176 nm (corresponding to a relative spectral width of 1.6 %). The calculated time-bandwidth product is about 0.4 which indicates Fourier-transform limited operation. Long IR pulses with narrow bandwidth can be obtained from a detuned U27 resonator (pulse duration of 3.4 ps with 0.4 % bandwidth).

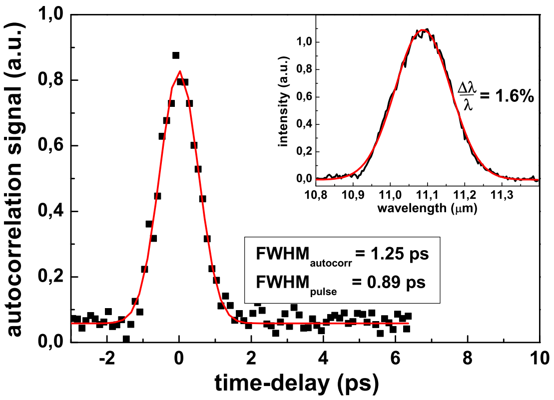


**Fig. 1** *Autocorrelation trace and the corresponding FWHM of the wavelength (inset) of 11 $\mu$m at maximum of the detuning curve of the FEL-U27.*

First pulse length measurements and corresponding spectra at different detuning points of the FEL-U100 [3] are shown in Fig. 2. Here we deduced the pulse duration by assuming a sech$^2$ temporal pulse shape, in contrast to a Gaussian pulse shape for the U27.

[1] J. Xu et al., Opt. Comm. 197 (2001) 379
[2] W. Seidel, IKH Annual Report 2004, FZR-423 (2005) 60
[3] Th. Dekorsy et al., IKH Annual Report 2004, FZR-423 (2005) 65

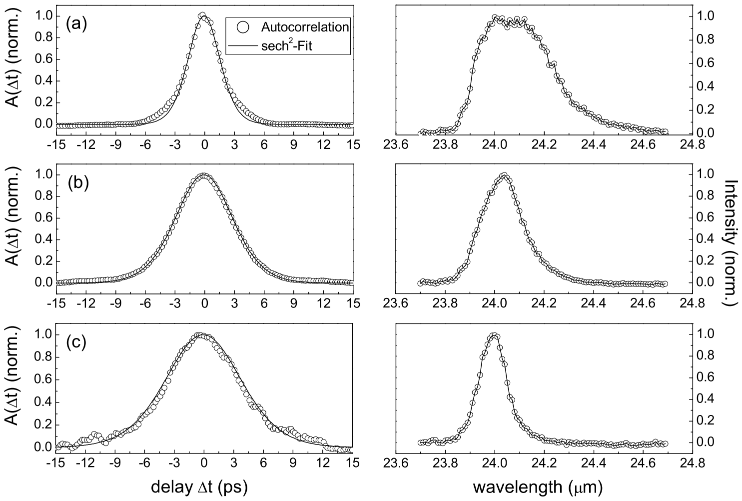


**Fig. 2** *Autocorrelation functions (left) and the corresponding spectra (right) for 24 $\mu$m radiation at three different detuned resonator lengths of the FEL-U100 (a: $\Delta L$=-2 $\mu$m, $FWHM_{pulse}$=2.5 ps; b: $\Delta L$=-14 $\mu$m, $FWHM_{pulse}$=4.4 ps; c: $\Delta L$=-24 $\mu$m, $FWHM_{pulse}$=5.8 ps).*

[1] *Inst. of Ion Beam Physics and Materials Research, FZD*

# Influence of the System Matrix on the Quality of the Reconstruction of In-Beam PET Data [E, G]

G. Shakirin, P. Crespo, W. Enghardt[1]

**Part of PhD thesis G. Shakirin, submitted to IEEE TNS**

At the experimental heavy ion therapy facility at the GSI Darmstadt an in-beam PET scanner is operated for quality assurance monitoring simultaneously to the therapeutic irradiation. A fully 3D maximum likelihood expectation maximization (MLEM) reconstruction algorithm has been developed and adapted to the special conditions of in-beam PET [1].

The system response function (system matrix) for that algorithm is implemented by separately calculating its components (geometry, scatter, attenuation and detector sensitivity). The geometry component of the system matrix is calculated "on-the-fly" during the reconstruction. In order to determine this component, the volume of each tube of response (TOR) is sampled by a number of lines whose endpoints are randomly distributed over the crystal surfaces. The number of lines used in the method is called a level. The higher the level, the more accurate and slower is the calculation.

We investigated the accuracy for this approach as well as for another method for calculating of the geometry component of the system matrix based on the approximation with splines [2]. An influence of the system matrix on the quality of reconstructed images was evaluated for MLEM and ordered subsets expectation maximization (OSEM) algorithms using real treatment data collected during the therapeutic irradiations at the GSI.

The accuracy of both methods for the system matrix calculation ("on-the-fly" and with splines approximation) was checked by means of analyzing the normalized mean square error (NMSE) (Fig.1 left). The method with splines approximation achieves high accuracy (NMSE $= 0.00047$) and performs with the same speed as "on-the-fly" method with level equal to 50. For visual comparison of accuracy the system matrix was calculated for one TOR with the two different methods (Fig. 1 right).

The influence of system matrix on the reconstruction quality was evaluated by means of an ensemble mean square error (EMSE) [3]. The true $\beta^{+}$-activity distributions were generated by means of the PosGen Monte Carlo code based on real treatment data of 9 patients. EMSE was calculated for reconstructions with the MLEM algorithm (50 iterations) and with the OSEM algorithm (8 subsets, 10 iterations). EMSE does not depend significantly on the quality of the system matrix when reconstructions are performed by MLEM algorithm, but significant deviations are observed when using the OSEM algorithm (Fig. 2).

As a conclusion, it is profitable to use the splines approximation method for reconstructions with OSEM algorithm where higher quality of the system matrix leads to lower mean square error and slightly better images. However, in the specific conditions of in-beam PET (dual-head geometry and low counting statistics) the best result for reconstructions performed by the MLEM algorithm by means of EMSE is achieved with the system matrix of poor quality (with "on-the-fly" method with level = 3) and visual comparison gives no significant difference.

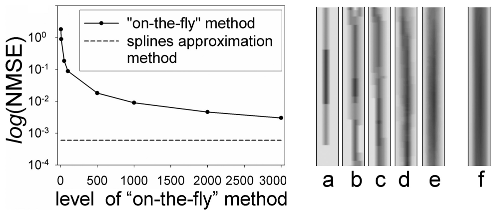


**Fig. 1** *Left: NMSE calculated for different levels for "on-the-fly" method comparing with NMSE for splines approximation method. Right: central slice of one TOR filled with system matrix values calculated with the "on-the-fly" method with level equal to 5 (a), 10 (b), 20 (c), 100 (d), 1000 (e) and with the splines approximation method (f).*

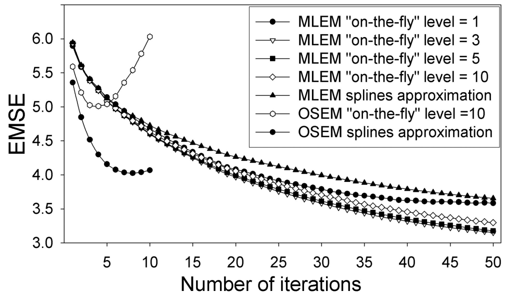


**Fig. 2** *EMSE for images reconstructed with MLEM and OSEM (8 subsets) algorithms and different methods for calculation of the system matrix.*

[1] K. Lauckner, Ph.D. Thesis, Technische Universität Dresden (1999)

[2] G. Shakirin, P. Crespo, W. Enghardt, GSI Sci. Rep. (2005) p. 394

[3] H. H. Barrett, K. J. Myers, ISBN: 0-471-15300-1 (2003) pp. 879-883

[1] *also TU Dresden*

## Optimum Voxel Size for Direct Time-of-Flight In-Beam PET [E,G]

G. Shakirin, P. Crespo, F. Fiedler, W. Enghardt[1], E. Grosse[1], A. Wagner

**Part of PhD thesis G. Shakirin**

The direct time-of-flight (TOF) reconstruction algorithm [1] can improve significantly the image quality for in-beam positron emission tomography (PET) [2] when applied to data measured with a tomograph having detectors with a coincidence time resolution of 100 ps (full width at half maximum). Such tomograph does not exist yet but its simulations are already feasible taking into account recent works on TOF detectors [3]. Typically, activity densities reached in fractionated carbon ion therapy are in the order of $200\ \mathrm{Bq\,cm^{-3}\,Gy^{-1}}$, resulting in low statistics datasets. We investigate the influence of the voxel size onto image quality by simulating two treatments with different irradiated volumes and statistics. A very large irradiated volume (pelvic chordoma, high image statistics, lower activity density), and a large head-and-neck irradiation (large image statistics, slightly larger activity density). For each case study a low-dose (fractionated radiotherapy ~0.6 Gy) and a high-dose (hypofractionation ~6 Gy) scenario is taken into account. For both cases and doses the generated $\beta^+$-activity distributions were simulated by means of the PosGen Monte Carlo code [4, 5].

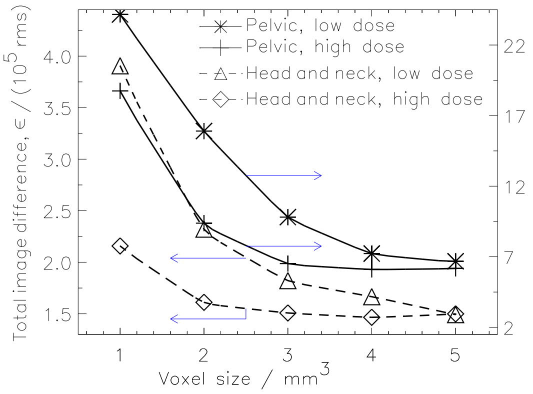


**Fig. 1** *Total image difference for the two study-cases considered. The root-mean-square (rms) difference of images obtained in each scenario (voxel size and dose) refers to the (not clinically feasible) image computed with a dose-enhancement factor of 1 000 (cf. Figs. 2 and 3, top rows).*

In order to find the optimum voxel size for each irradiation scenario, Fig. 1 was constructed. It shows the differences obtained between images reconstructed with several voxel sizes and a reference image obtained with ultra-high (~600 Gy) statistics. It can be seen that for a low-dose pelvic irradiation an optimum voxel size yielding the minimum deviation lies at $(5\ \mathrm{mm})^3$. Fig. 2 confirms that, in this situation, the small loss of spatial resolution still suffices to monitor sensitive organs (colon) lying close to the irradiated volume (tumor). For monitoring low-dose head-and-neck treatments a higher spatial resolution is required due to the finer structures present in the skull (Fig. 3). Despite Fig. 1 pointing to smaller deviations with an image voxel of $(5\ \mathrm{mm})^3$, visual inspection of the reconstructed images introduces an optimum voxel size of $(3\ \mathrm{mm})^3$ in order to conserve the spatial resolution required to monitor finer anatomic structures (Fig. 3).

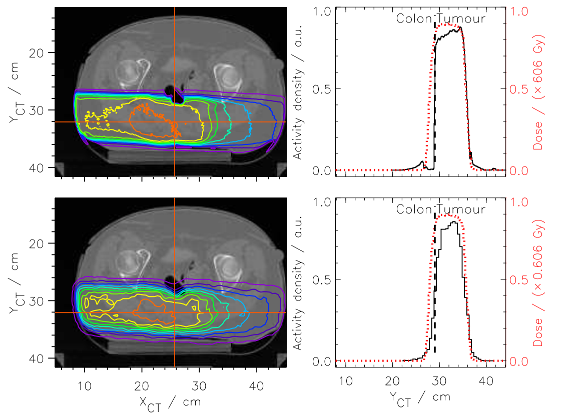


**Fig. 2** *Pelvic irradiation. Top: very-high activity density (simulated dose enhanced by 1 000), sampled with 1 mm³ voxel. Botom: low-dose scenario reconstructed with a simulated, dual-head, direct TOF tomograph with (5 mm)³ image voxel. All images submitted to a 3D median filter.*

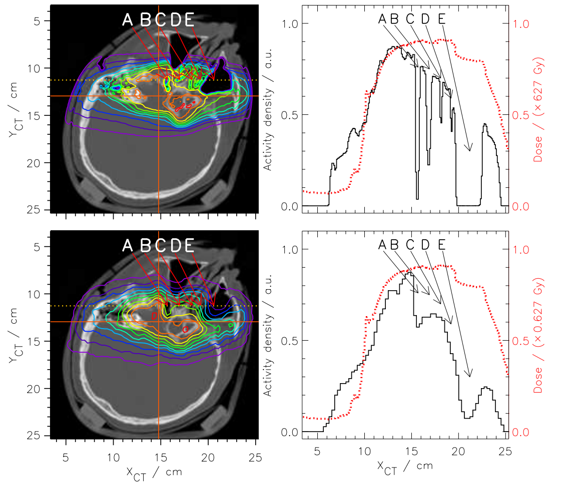


**Fig. 3** *Head-and-neck irradiation. Simulated dose and reconstruction details like in Fig. 2, except for the (3 mm)³ voxel size of the low-dose scenario (bottom). The arrows indicate fine structures of the skull: sphenoidal sinus (A), right (B), left (C and D) posterior meatus, and left maxillary sinus (E).*


[1] P. Crespo et al., Phys. Med. Biol. to be submitted

[2] W. Enghardt, P. Crespo et al., NIM A 525 (2004) 284

[3] J. Glodo, A. Kuhn et al., IEEE Nucl. Sci. Symp., 2006

[4] B.G. Hasch, Thesis, Technische Universität Dresden, 1996

[5] F. Pönisch, K. Parodi et al., Phys. Med. Biol. 49 (2004) 5217


[1] *also TU Dresden*

# In-Beam PET Measurements of Biological Half-Lives of $^{12}$C Irradiation Induced $\beta^+$-Activity [E,G]

**F. Fiedler, M. Sellesk [1], P. Crespo, R. Jülich,** K. Parodi[2], **J. Pawelke, F. Pönisch, W. Enghardt [3]**

**Part of PhD thesis F. Fiedler**

**Introduction**

The in-beam PET method is a valuable tool to measure the distribution of the delivered dose in the irradiated tissue in carbon ion therapy which has so far been applied to more than 300 patients. In order to evaluate the PET data with respect to the patient anatomy, positioning and range of the beam [1], they need to be compared with a simulation of the expected activity distribution [2]. Although these algorithms are well adapted to the therapeutic situation, there are differences that can be attributed to metabolic processes taking place in living organisms, such as the predominant perfusion-driven washout of the positron emitters. Since comprehensive data of the washout as a function of the tissue and the type of the radionuclides are not available, these processes are not taken into account in the current simulation code. In order to obtain such data, we analysed the results of a set of in-beam PET data scans taken during therapeutic $^{12}$C irradiation.

**Patient studies**

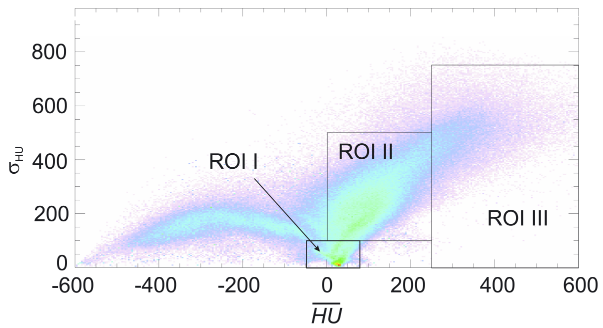


**Fig. 1** *Two-dimensional histogram of the fraction of the LOR intersecting the planned target volume as a function of $\overline{HU}$ and $\sigma_{HU}$. The corresponding anatomical regions for a particular patient can be seen in Fig. 2.*

We expect a correlation between the tissue type along the lines of response (LOR) of the positron camera and the effective half life. The only available information in this respect is provided by the planning CT, i.e. the Hounsfield unit (HU). However, the mean HU, $\overline{HU}$, along a LOR is not sufficient for classification, the standard deviation of the HU within each LOR ($\sigma_{HU}$) was additionally introduced to take into account tissue inhomogeneity (cf. Fig. 1). These two quantities were classified into 3 different regions of interest (ROI) for 14 patients. ROI I was supposed to contain rather homogeneous brain tissue (e.g. brain), ROI II was expected to include soft, but inhomogeneous tissue, and ROI III was for bone. The anatomical mapping is displayed in Fig. 2. No dependence of the effective half life on the $\overline{HU}$ and $\sigma_{HU}$ was found.

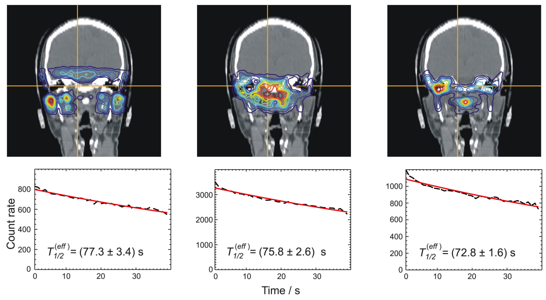


**Fig. 2** *Effective half-lives in the patient according to the ROIs defined in Fig. 1. The left figure corresponds to ROI I, the middle to ROI II and the right to ROI III, respectively.*

Therefore, we investigated the effect of the different dose levels on the effective half live by analysing two other groups of LOR. The first contained at least ten voxels with 90 % of the maximum dose. The second set of LOR contained voxel with 0 - 90 % of the maximum dose with no voxel higher than 90 %. Combining data of 55 patients, a lower effective half live for the 0 - 90 % region was found ($T_{1/2} = 71.8 \pm 0.6$ s) than for the 90 - 100 % region ($T_{1/2} = 79.5 \pm 1.8$ s) possibly due to less perfusion in the tumour. **Conclusions** The in-beam PET data acquired during 40 s after finishing therapeutic irradiation indicate that on this rather short time scale no differentiation of tissue with respect to the washout rate of the $^{12}$C beam induced $\beta^+$-radioactivity was observed. Therefore, if in-beam PET measurements can be restricted to scanning times below 100 s, the influence of tissue dependent washout processes to the spatial distribution of beam induced $\beta^+$-activity can be expected to be drastically diminished. This is expected to improve the correspondence between the measured in-beam PET images and those predicted from the treatment plan.

[1] W. Enghardt, P. Crespo et al., Nucl. Inst. Meth. A 525 (2004), 284.

[2] F. Pönisch, K. Parodi et al., Phys. Med. Biol. 49 (2004) 5217.

[1] *also TU Bergakademie Freiberg*
[2] *Ionenstrahl-Therapiezentrum Heidelberg*
[3] *also TU Dresden*

# The Feasibility of In-Beam PET for Therapeutic Beams of $^3$He [G,E]

F. Fiedler, P. Crespo, K. Parodi[1], M. Sellesk[2], W. Enghardt[3]

**Published in IEEE Transactions on Nuclear Science 53 (2006) 2252**

At the experimental carbon ion treatment facility at the Gesellschaft für Schwerionenforschung (GSI) Darmstadt the clinical benefit of the in-beam PET method has been proven. It led to a significant improvement of the quality of patient treatment. Several heavy ion treatment facilities, which will provide in the near future a large variety of ions, are in planning or even under construction. The deduction of clinically relevant parameters from in-beam PET data requires a precise knowledge of the spatial distribution of beam induced positron emitters in the irradiated volume. Therefore, the $\beta^+$-activity induced by $^3$He has been studied for the first time at the Gesellschaft für Schwerionenforschung with three mono-energetic $^3$He beams of 130.03 $A$MeV to 207.92 $A$MeV and mean intensities varying from $2.0 \cdot 10^8$ to $3.5 \cdot 10^8$ ions / s. The beams were stopped in homogeneous thick targets consisting of PMMA, graphite and water, which were placed in the center of the field of view of the PET-scanner at the experimental carbon ion therapy at GSI. Results on the production rate and the spatial distribution of $^3$He ion induced positron activity is presented and compared with data from $^{12}$C-irradiation (cf. Fig. 1). The accuracy and resolution for determining the range of the $^3$He primary beams is deduced. Furthermore, energy dependent thick target cross sections for different reaction channels leading to positron emitters are estimated from the experimental data (cf. Fig. 2).

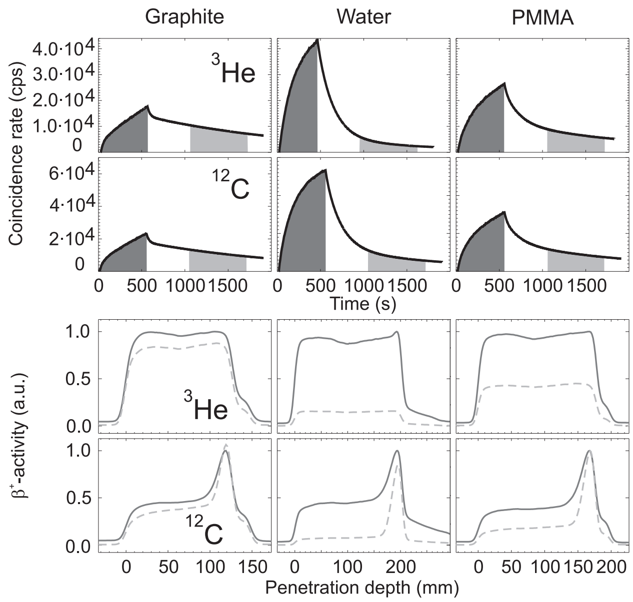


**Fig. 1** *Time-event histograms and depth profiles of $\beta^+$-activity induced by $^3$He and $^{12}$C-beams at 207.92 AMeV and 337.5 AMeV, respectively, in graphite (left), water (middle) and PMMA (right) targets. 1st row: Measured time-event-histograms for $^3$He-ions. 2nd row: As 1, but for $^{12}$C-projectiles. 3rd row: $\beta^+$-activity depth profiles for $^3$He-ions. The solid lines display the activity measured during the irradiation (left marked area in 1st row), the gray dashed lines (right marked area in 1st row) give the activity from 10 to 20 min after the end of the irradiation normalized to the maximum of the activity measured during the irradiation. The ordinate is in arbitrary units. 4th row: as 3, but for $^{12}$C-projectiles. In the case of $^{12}$C-projectiles the main contribution coming from the projectile fragments is nearly the same in both periods. In case of a graphite target there is a slightly higher signal for the decay measurement due to the longer measuring time. The mentioned absence of projectile fragments in case of $^3$He-projectiles leads to a larger difference in the counting statistics between these two time intervals. For the water target the largest difference was observed due to the short half life of the dominating positron emitter, $^{15}$O. Since human tissue consists of about 65% of water the importance of measuring during the irradiation by means of in-beam PET increases when going to projectiles which do not form $\beta^+$-emitting fragments.*

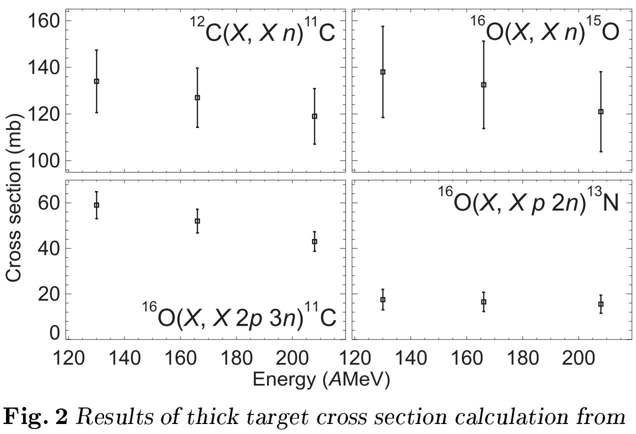


**Fig. 2** *Results of thick target cross section calculation from experimental data. Additionally the cross section of the reaction $^{12}C(X,\ X\ 2n)^{10}C$ was found to be $(9.0 \pm 1.5)$ mb. The reactions are mainly induced by $^3He$, but there are also non-negligible contributions coming from reactions with secondary particles like protons, deuterons and neutrons, thus $X = \{^3He, p, n, d\}$. Furthermore, in the exit channel $X = \{^3He, d\}$ the deuteron may be disintegrated into nucleons.*

[1] *Ionenstrahl-Therapiezentrum Heidelberg*
[2] *also TU Bergakademie Freiberg*
[3] *also TU Dresden*

# In-beam PET at High-Energy Photon Beams: A Feasibility Study

H. Müller, W. Enghardt[1]

**Published in Phys. Med. Biol. 51 (2006) 1779-1789**

For radiation therapy with carbon ion beams, either of the stable isotope $^{12}$C or of the radioactive one $^{11}$C, it has been demonstrated that the $\beta^+$-activity distribution created or deposited, respectively, within the irradiated volume can be visualised by means of positron emission tomography (PET). Those PET images provide valuable information for quality assurance and precision improvement of ion therapy. Dedicated PET scanners have been integrated into treatment sites at HIMAC (Japan) and GSI (Germany) to make PET imaging feasible during therapeutic irradiation (in-beam PET). A similar technique may be worthwhile for radiotherapy with high-energy bremsstrahlung. In addition to monitoring the dose delivery process which in-beam PET has been primarily developed for, it may be expected that radiation response of tissue can be detected by means of in-beam PET. We investigate the applicability of PET for treatment control in case of using bremsstrahlung spectra produced by 15 - 50 MeV electrons. Target volume activation due to $(\gamma, n)$ reactions at energies above 20 MeV yields moderate $\beta^+$-activity levels, which can be employed for imaging. The radiation from positrons produced by pair production is not presently usable because the detectors are overloaded due to the low duty factor of medical electron linear accelerators. However the degradation of images caused by positron motion between creation and annihilation seems to be tolerable.

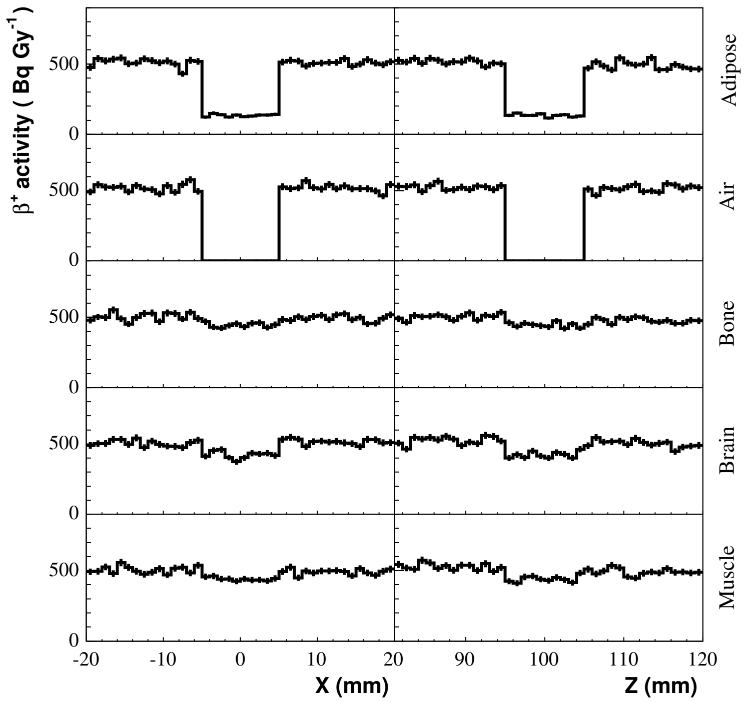


*Distribution of $\beta^+$ activity deposited transverse (X) (left panel) and longitudinal (Z) right panel) to the beam direction for various types of tissues embedded in water as indicated the figure. The hard variant of the 50 MeV spectrum has been used for the calculations. The vertical bars represent the statistical errors.*

[1] *also TU Dresden*

# Results of First Experiments on In-Beam PET at 34 MV Bremsstrahlung Beams[E]

D. Möckel, T. Kluge, J. Pawelke, W. Enghardt[1]

**Part of PhD thesis D. Möckel and part of Diploma thesis T. Kluge**

Since there are good experiences with in-beam PET for quality assurance in carbon ion therapy [1] it is highly desirable to extend this method to other radiation treatment modalities. For example, in-beam PET seems to be feasible for high energy photon irradiation with energies above $\sim 20$ MeV because of the generation of positron emitters in tissue (predominantly $^{11}$C and $^{15}$O) by $(\gamma, n)$ reactions as already shown in simulations [2]. First experimental studies concerning the measurement of photon induced activity distribution have already been done by means of off-beam PET experiments [3]. In these investigations only the $^{11}$C activity distribution could be measured, since the time interval between irradiation and measurement was about 15 half-lives of $^{15}$O. To shorten this time interval by combining irradiation and measurement and thus to increase the measured activity, an in-beam measuring setup, adapted from the PET scanner for education presented in [4], was built up at ELBE.

The irradiation setup is similar to that used in the off-beam PET experiments. Additionally, for coincident registration of the annihilation photons of the generated positron emitters, two commercial BGO block detectors (ECAT EXACT, Siemens) have been mounted face-to-face at a distance of $\sim 30$ cm with the phantom between them. They are coupled and moved linearly in beam direction. So during the irradiation the detectors scan a selected region several times. The list mode data acquisition proceeds continuously during the movement. After each scan the data are reconstructed and a two-dimensional image of the measured activity distribution is obtained. Various homogeneous as well as inhomogeneous phantoms were irradiated by 34 MV bremsstrahlung. The generated activity distribution was measured simultaneously. During irradiation not only positrons from $(\gamma, n)$ reactions are emitted but also a high number of positrons produced by pair production [2]. Their signals in combination with the high radiation background at the irradiation site lead to an overloading of the detectors. Therefore, the accelerator was operated in macropulse mode and data were only acquired in the macropulse pauses.

By means of the performed in-beam PET experiments the $^{11}$C and $^{15}$O activity distributions could be measured. Higher activity concentrations are determined in comparison to the off-beam PET experiments depending on the oxygen content. Due to the different half-lives of $^{11}$C and $^{15}$O ($T_{1/2}(^{11}\mathrm{C}) = 20.38$ min, $T_{1/2}(^{15}\mathrm{O}) = 2.03$ min) a good contrast between materials with various density values and stoichiometry can be achieved. One example is shown in Fig. 1. The two-dimensional activity distribution as well as a schematic representation of an inhomogeneous, tissue equivalent phantom, irradiated by 34 MV bremsstrahlung, is displayed.

Since the coincidence events are acquired in list mode the activity in dependence on the measuring time could be investigated, too. The time course of the activity shows the production during and the decay after the irradiation in dependence on the carbon and oxygen content (cf. Fig. 2).

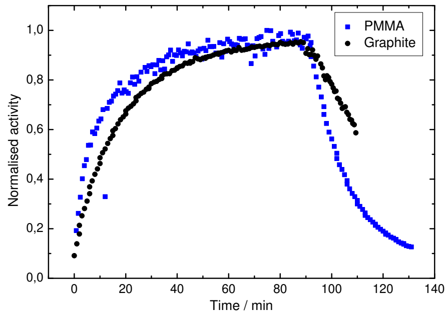


**Fig. 2** *Production and decay of activity, generated by 34 MV bremsstrahlung, for PMMA and graphite.*

[1] W. Enghardt, P. Crespo et al., Nucl. Instr. Meth. A 525 (2004) 284

[2] H. Müller and W. Enghardt, Phys. Med. Biol. 51 (2006) 1779

[3] D. Möckel, J. Pawelke et al., IKH Annual Report 2005, FZR-442 (2006) 59

[4] T. Würschig and W. Enghardt, IKH Annual Report 2005, FZR-442 (2006) 60

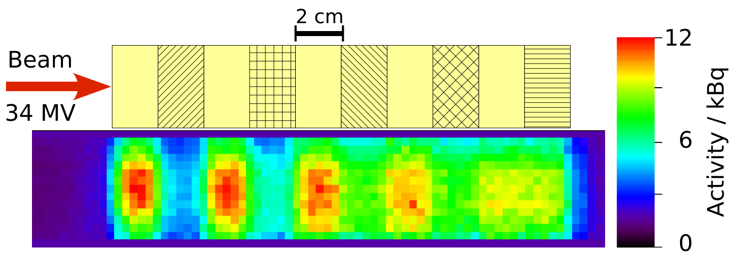


**Fig. 1** *Schematical illustration (top) as well as two-dimensional distribution of the generated positron emitters ($^{11}C$ and $^{15}O$) in an inhomogeneous phantom for an electron energy of 34 MeV (bottom).*

[1] *also TU Dresden*

# Electron Beam Monitoring for Channeling Radiation Measurements

W. Neubert, B. Azadegan, W. Enghardt, K. Heidel, J. Pawelke, W. Wagner

**Published in Nucl. Instr. Meth. B 254 (2007) 319-328**

A secondary emission monitor (SEM) and an auxiliary Faraday cup necessary for calibration purposes (Fig. 1) have been constructed and installed at the radiation physics beam line of ELBE. These devices are to be applied for the precise beam-current monitoring in measurements of channeling radiation. Miscellaneous simulations of underlying interactions of the beam electrons with the target material as well as with the materials of the monitor equipment have been performed to optimize the design and to evaluate possible correction factors inherent to transmission monitoring (Fig. 2).

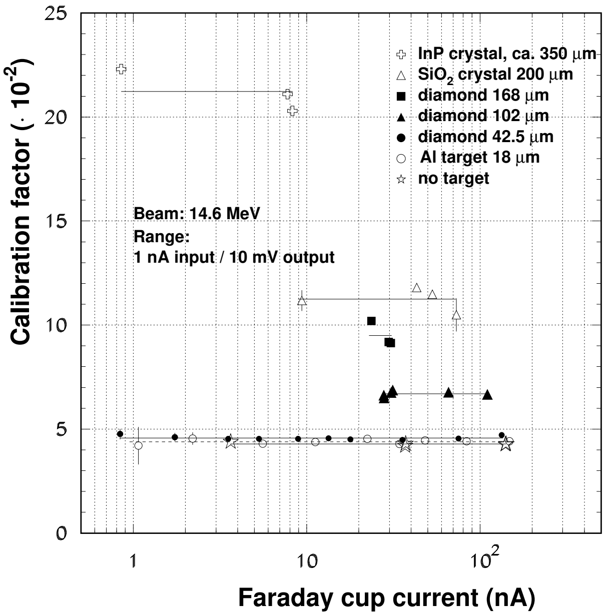


**Fig. 1** *Calibration factors of the SEM for different targets in dependence on the beam current determined by means of the Faraday cup. The data are not corrected for beam losses due to multiple scattering.*

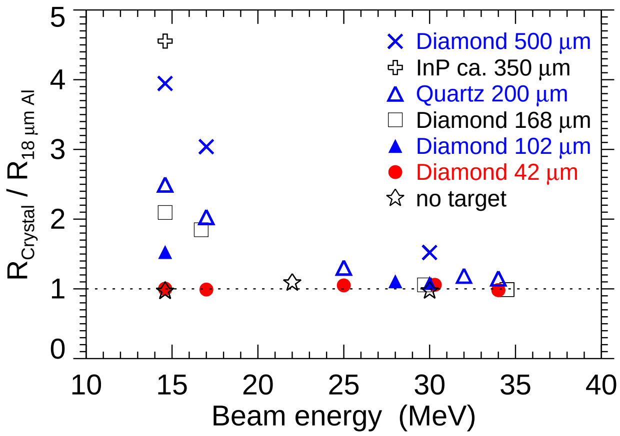


**Fig. 2** *Experimentally determined relative calibration factors of the SEM used for beam current monitoring in measurements of channeling radiation.*

# Investigation of Planar Channeling Radiation from Different Plane of Quartz

B. Azadegan, W. Wagner, J. Pawelke

**Part of PhD thesis B. Azadegan**

First results of measurements of planar electron channeling radiation (CR) on quartz are presented in Ref. [1]. The stimulation of CR by ultrasonic vibrations excited in piezoelectric crystals has been considered in Refs. [2, 3]. The observation of predicted phenomena such as CR line splitting or even selective intensity amplification, however, requires the detailed knowledge of the transverse electron states in the crystal planes of quartz. The spectrometry of CR on quartz provides information about the suitability of different crystal planes for the ultrasonic stimulation of CR. Therefore, we performed systematic measurements of CR from different planes of quartz.

The analysis of the measurements bases on the application of the theory of CR. Real planar continuum potentials of quartz, transition energies, line widths and relative intensities have been calculated. Compared with the CR observed on monatomic crystals (e.g. diamond or Si), which have a more simple cubic structure, the registration of CR on quartz is to some degree complicated by the large variety of closely adjacent planes in the hexagonal lattice of this binary crystal. For illustration of this feature, the zone of the x-cut axis $[2\bar{1}\bar{1}0]$ of $\alpha$-quartz is shown in Fig. 1. The planes, in which CR has been generated, are given by full lines. No CR has been observed from planes given by dashed lines

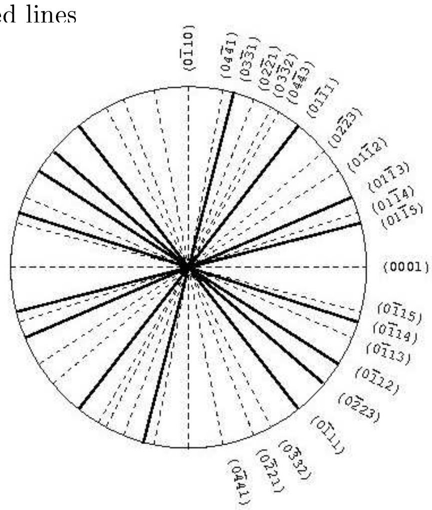


**Fig. 1** *Zone of the $[2\,\bar{1}\,\bar{1}\,0]$ axis of quartz.*

The CR spectra from 32 MeV electrons channeled in the $(01\bar{1}1)$ and $(0\bar{1}11)$ planes are shown in Figs. 2 and 3, respectively, together with the calculated planar potentials. The calculated transition energies between bound states are indicated by vertical bars, the heights of which have been chosen proportional to the transition rates assuming equilibrium initial population of states.

According to Refs. [2, 3], these two planes are probably suitable candidates for some observation of CR stimulated by ultrasonic waves with frequencies of $\leq 10$ GHz.

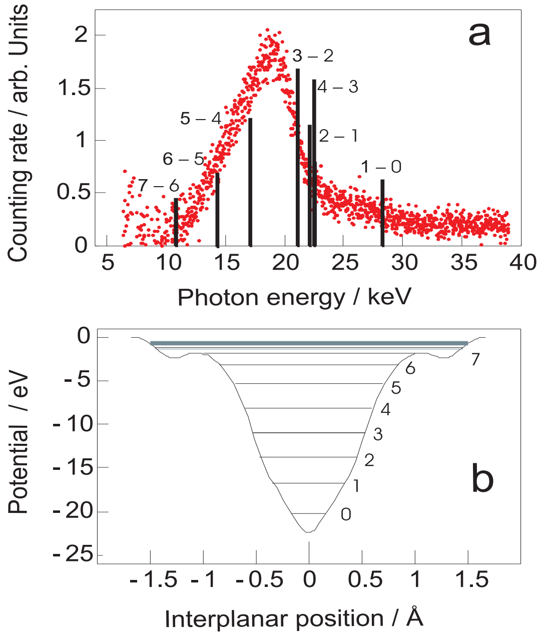


**Fig. 2** *Background corrected spectrum of planar CR observed for 32 MeV electrons channeled along the $(0\,1\,\bar{1}\,1)$ plane of quartz (a) and the corresponding planar potential (b).*

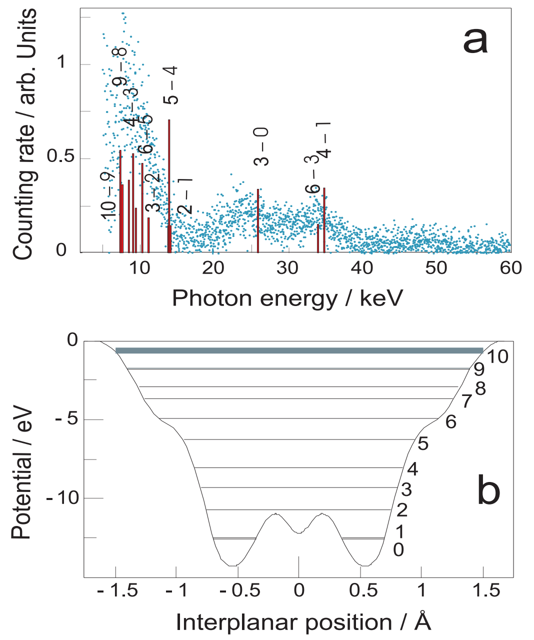


**Fig. 3** *Analogous to Fig. 2 but for the $(0\,\bar{1}\,1\,1)$ plane.*

[1] B. Azadegan, W. Wagner, J. Pawelke, L.Sh. Grigoryan, IKH Annual Report 2005, FZR-442 (2006) 66

[2] L.Sh. Grigoryan et al., Nucl. Instrum. Meth. B 173 (2001) 184

[3] L.Sh. Grigoryan et al., Nucl. Instrum. Meth. B 212 (2003) 51

# Dependence of the Linewidth of Planar Electron Channeling Radiation on the Thickness of the Diamond Crystal

B. Azadegan, W. Wagner, J. Pawelke

**Published in Phys. Rev. B 74 (2006) 045209, 1-11**

Measurements of (110) planar channeling radiation have been performed at the radiation source ELBE at electron energies of 14.6, 17, 30 and 34 MeV using diamond crystals of thickness 42.5, 102, 168 and 500 $\mu$m. The influence of different line-broadening mechanisms on the spectral shape of radiation from the 10 transition has been investigated. The analysis bases on fitting a convolution of the intrinsic Lorentz-like line shape with a Gaussian-like multiple-scattering distribution to the measured spectra (Fig. 1). The asymmetry parameter ($\alpha$) involved relates to the standard deviation of the effective multiple-scattering angle. Its dependence on the crystal thickness was found to be weaker than for nonchanneled particles (Fig. 2). The deduced coherence lengths show no significant dependence on the electron energy.

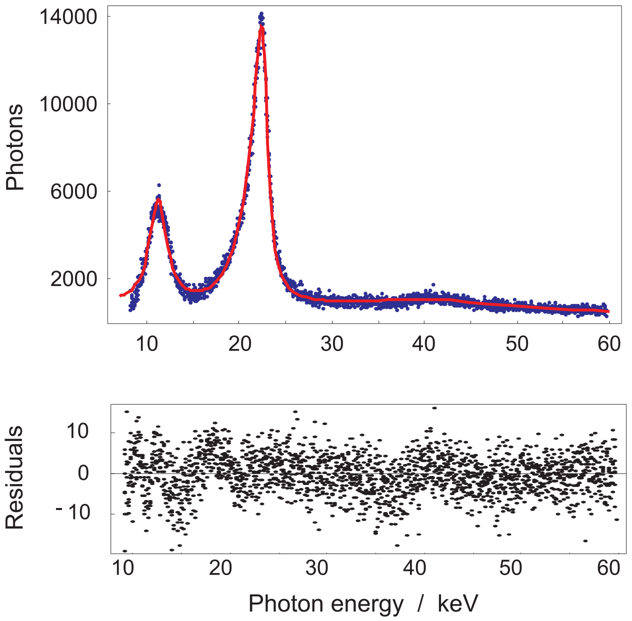


**Fig. 1** *Upper panel: Measured spectral distribution of (110) planar channeling radiation for a 168 $\mu$m thick diamond crystal at an electron energy of 17 MeV (blue). Two asymmetric line profiles and a polynomial background distribution were fitted to the spectrum (red). Lower panel: Residuals between the measured and the approximated distribution.*

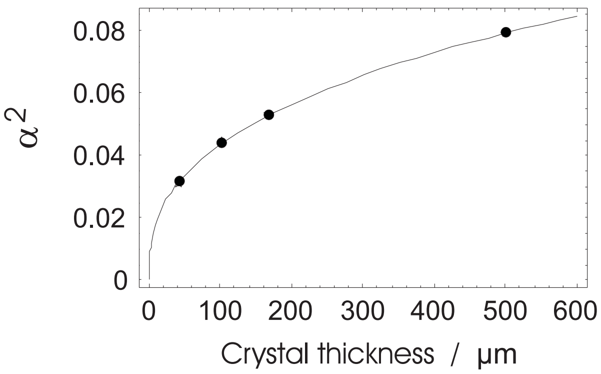


**Fig. 2** *Dependence of the squared line-asymmetry parameter on the crystal thickness.*

# RBE of 25 kV X-Rays for the Survival and Induction of Micronuclei in the Human Mammary Epithelial Cell Line MCF-12A

A. Lehnert, E. Lessmann, J. Pawelke, W. Dörr[1]

**Published in Radiat. Environ. Biophys. 45 (2006) 253-260**

The broad application of low energy X-rays below about 50 keV in radiation therapy and diagnostics and especially in mammography substantiates the precise determination of their relative biological effectiveness (RBE). A quality factor of 1 is stated for photons of all energies in the ICRP Recommendations. However, the RBE of low-energy X-rays compared to high-energy photons was found to be dependent on photon energy, cell line and endpoints studied, hence varying from less than 1 up to about 4. In the present study, the human mammary epithelial cell line MCF-12A has been chosen due to the implementation of the results in the estimation of risk from mammography procedures. The RBE of 25 kV X-rays (W anode, 0.3 mm Al filter) relative to 200 kV X-rays (W anode, 0.5 mm Cu filter) was determined for clonogenic survival in the dose range 1–10 Gy and micronuclei induction in the range 0.5–3.5 Gy. The RBE for clonogenic survival was found to be significantly higher than 1 for surviving fractions in the range $0.005 < S < 0.2$. The RBE decreased with increasing survival, with an $RBE_{0.1}$ at 10 % survival of $1.13 \pm 0.03$. The effectiveness of soft X-rays for micronuclei induction was found to be $1.40 \pm 0.07$ for the fraction of binuclear cells (BNC) with micronuclei (MN) and $1.44 \pm 0.17$ for the number of MN per BNC (cf. Fig. 1). In contrast, the RBE determined from the number of MN per MN-bearing BNC was found to be $1.08 \pm 0.32$. This indicates that the effectiveness of 25 kV X-rays results from an increase in the number of damaged cells, which, however, do not have higher number of micronuclei per cell.

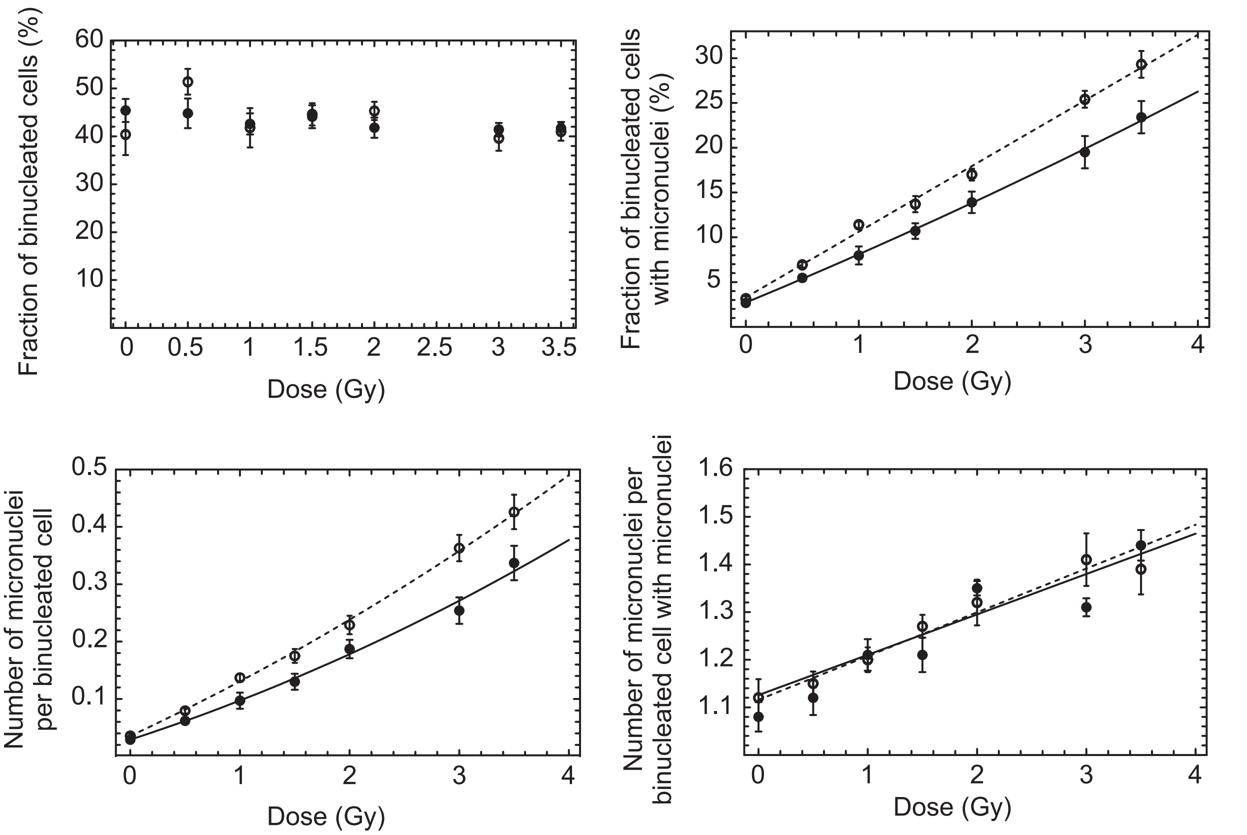


**Fig. 1** *Dose response of micronuclei induction after irradiation of MCF-12A cells with 25 kV X-rays (open circles, dashed lines) and 200 kV X-rays (closed circles, solid lines). The fraction of BNC (top, left), fraction of BNC with MN (top, right), number of MN per BNC (bottom, left) as well as the number of MN per MN-bearing BNC (bottom, right) are presented. The mean values and the SEM from 6 experiments are shown.*

[1] *TU Dresden*

# Repair Kinetics of DNA Double Strand Breaks Induced in Human Mammary Epithelial Cells

E. BEYREUTHER, W. DÖRR[1], E. LESSMANN, J. PAWELKE

**Part of PhD thesis E. Beyreuther**

The introduction of mammography screening programs in some countries initiated a continuous discussion about the benefit or possible accompanied risk of the used radiation qualities. Contributing to this discussion we used different methods, such as clonogenic survival and the analysis of chromosomal aberrations by Fluorescence in situ Hybridisation (FISH), to study biological effects with the human mammary epithelial cell line 184A1, which is of interest especially for the induction of breast cancer. Radiation qualities applied were 10 and 25 kV soft X-rays and a 200 kV X-ray tube as reference radiation source. Furthermore, we develop these methods and investigate the repair kinetics of DNA double strand breaks (DSB) with cell line 184A1 to learn more about underlying processes.

The DNA damage response, following irradiation, includes an efficient DSB recognition system as well as different DSB repair mechanisms. Important contributions to these processes are the phosphorylation of histone H2AX ($\gamma$H2AX) and the localization and phosphorylation of the p53 binding protein 1 (53BP1) at the sides of DNA DSBs. Both molecules are essential for the recognition of DNA DSBs and hence for the induction of repair processes. Using appropriate antibodies, the phosphorylated molecules can be visualized as nuclear foci and their time-dependent formation can be followed after irradiation.

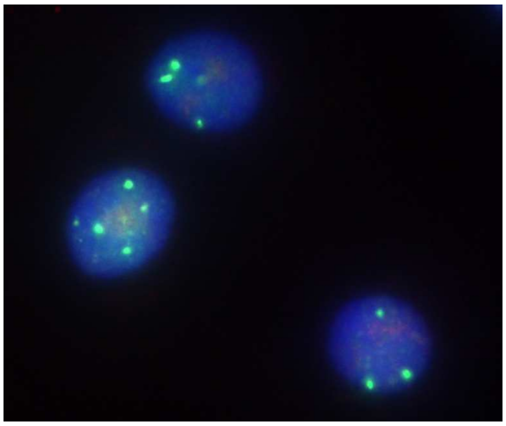

**Fig. 1** *Marked foci of cell line 184A1, induced by 25kV X-rays and observed 2 hours after irradiation*

The time-dependent formation of $\gamma$H2AX- and 53BP1-foci, was used to investigate the induction and rejoining of DNA DSBs up to 48 hours after irradiation. Two different antibodies and their corresponding fluorochromes were used to visualize and quantify the foci induced by two different doses of 0.25 and 2 Gy for 25 and 200 kV X-rays, respectively.

The kinetics obtained after irradiations with 2 Gy show a similar shape and therefore energy independence for both energies, which can be explained by the same underlying repair processes. Shortly after irradiation the number of foci per cell shows a steep increase, resulting in a maximum after 2 hours and a subsequent 2-phase decrease.

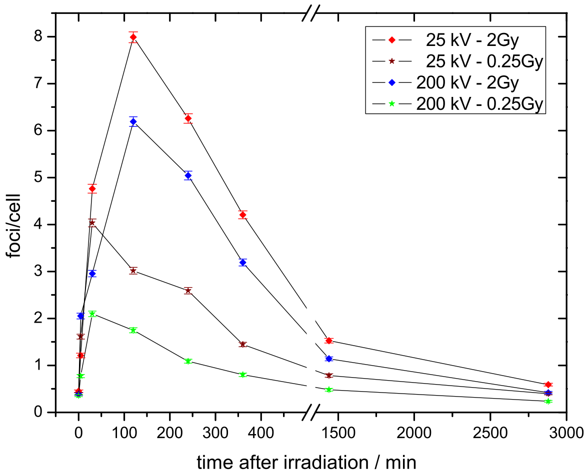


**Fig. 2** *Kinetics of the DNA DSB induced by 0.25 and 2 Gy of 25 kV and 200 kV X-rays.*

Although the position of the maximum is the same, the number of foci per cell differs for 25 kV and 200 kV X-rays, being 7.99 ± 0.12 and 6.19 ± 0.10, respectively. The rejoining of DSBs, deduced by the decrease of number of foci per cell, can be divided in a first phase, which seems to be faster, and a slower second one. During the first phase, the number of foci per cell is reduced to about 50% of the maximum and in the second phase they are reduced to the control level, whereas for 25 kV a significant number of foci per cell remain. These results implicate that, on the one hand, the number of the induced DNA DSBs is significantly higher for 25 kV X-rays and, that on the other hand, some DSBs remain unrepaired. These DSBs can influence the genomic integrity and can result in chromosomal aberrations.

The experiments for the irradiations with 0.25 Gy for both energies show the same shape as that with higher dose, but the maximum is derived at 30 minutes after irradiation. The maximum number of foci per cell was 4.03 ± 0.08 for 25 kV and 2.10 ± 0.06 for 200 kV X-rays, which is about the half or less compared to the results of 2 Gy with the same energies.

[1] *TU Dresden*

## AMOS - An Effective Tool for Adjoint Monte Carlo Photon Transport [D]

D. Gabler[1], J. Henniger[1], **U. Reichelt**

**Published in Nucl. Instr. Meth. B 251 (2006) 326-332**

In order to expand the photon version of the Monte Carlo transport program AMOS to an adjoint photon version, AMOS Pt, the theory of adjoint radiation transport is reviewed and evaluated in this regard. All relevant photon interactions, photoelectric effect, coherent scattering, incoherent scattering and pair production, are taken into account as proposed in the EPDL 97. In order to simulate pair production and to realise physical source terms with discrete energy levels, an energy point detector is used. To demonstrate the qualification of AMOS Pt a simple air-over-ground problem is simulated by both the forward and the adjoint programs. The results are compared and total agreement is shown (Fig. 1 and Fig. 2).

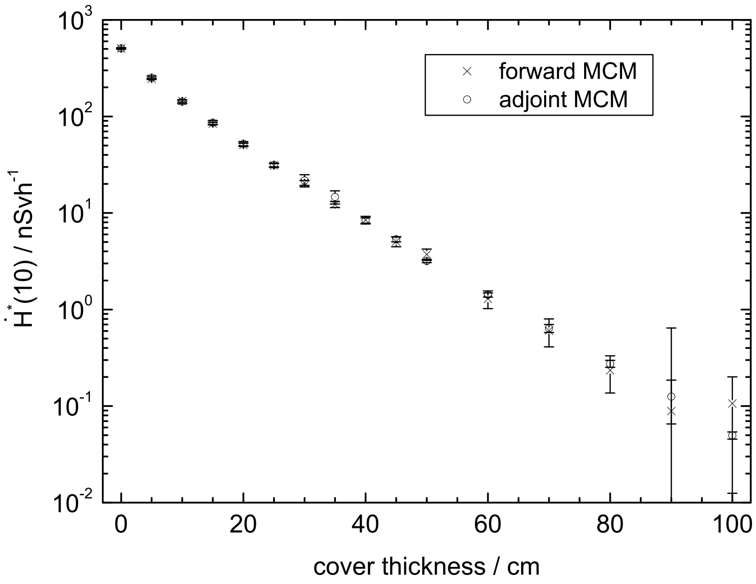


**Fig. 1** *Comparison of forward and adjoint results for the ambient dose equivalent rate of the air-over-ground problem. Therein a small detector is positioned over a infinite source distribution covered by a soil layer of variable thickness.*

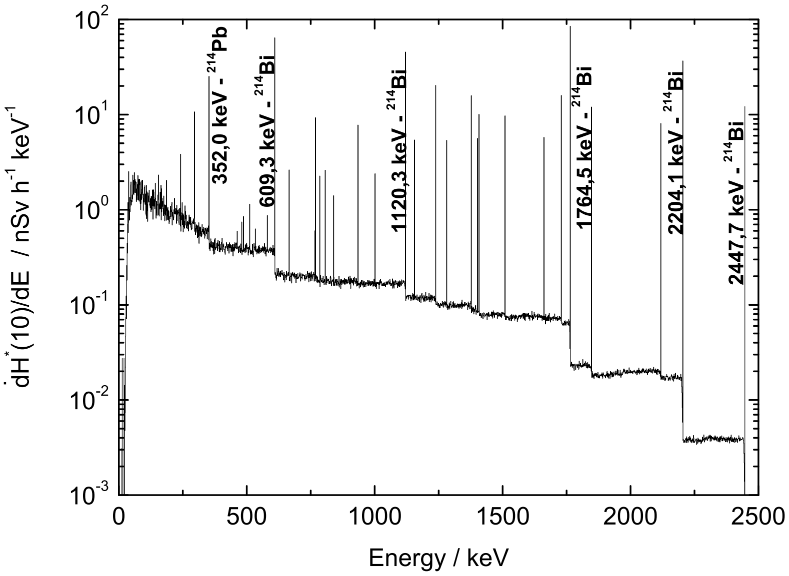


**Fig. 2** *Adjoint simulated spectrum of the ambient dose equivalent rate for a cover thickness of 0 cm. The corresponding nuclides for some dose peaks are added.*

[1] *TU Dresden*

# Application of Advanced Monte Carlo Methods in Numerical Dosimetry D

**U. Reichelt**, J. Henniger[1], C. Lange[1]

**Published in Radiat. Prot. Dosim. 119 (2006) 479-482**

Many tasks in different sectors of dosimetry are very complex and highly sensitive to changes in the radiation field. Often, only the simulation of radiation transport is capable of describing the radiation field completely. Down to sub-cellular dimensions the energy deposition by cascades of secondary electrons is the main pathway for damage induction in matter. A large number of interactions take place until such electrons are slowed down to thermal energies. Also for some problems of photon transport a large number of photon histories need to be processed. Thus the efficient non-analogue Monte Carlo program, AMOS, has been developed for photon and electron transport. Various applications and benchmarks are presented showing its ability. For radiotherapy purposes the radiation field of a brachytherapy source is calculated according to the American Association of Physicists in Medicine Task Group Report 43 (AAPM/TG43) (see Fig. 1). As additional examples, results for the detector efficiency of a high-purity germanium (HPGe) detector (Fig. 2) and a dose estimation for an X-ray shielding for radiation protection are shown.

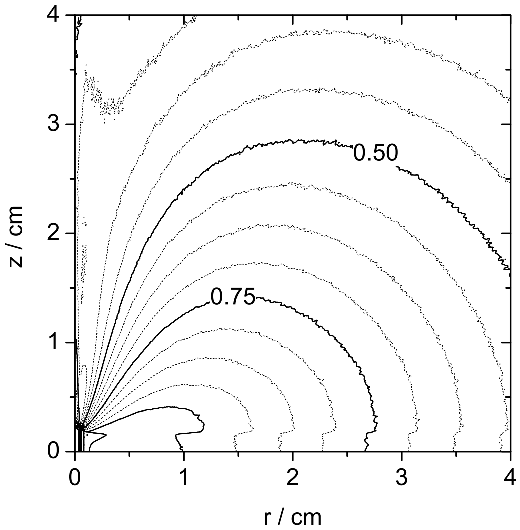


**Fig. 1** *Relative dose distribution in surrounding water of a cylindrical $^{125}$I Bebig brachy therapy source designed for interstitial cancer therapy of prostate gland.*

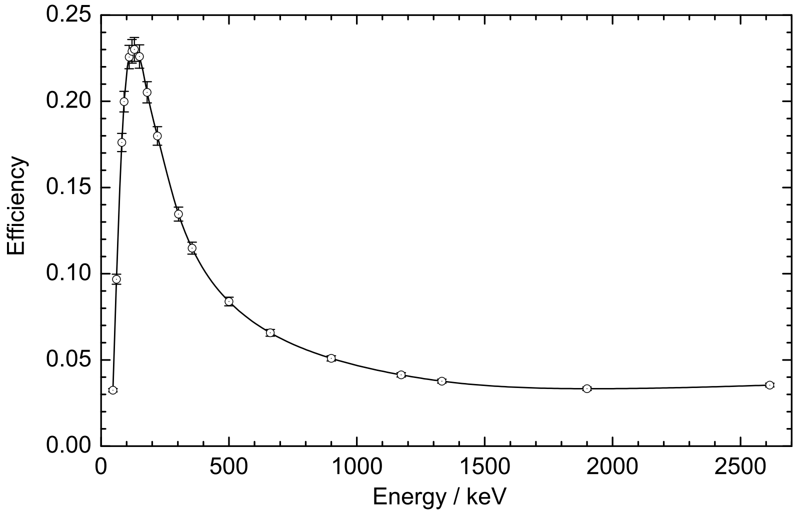


**Fig. 2** *Simulated peak efficiency of full energy events for a HPGe detector.*

[1] *TU Dresden*